Supplementary Information for

Multi-stimulated far-UVC luminescence for solar-blind imaging

Chongyang Cai[1], Leipeng Li[1,*], Xiaohuan Lv[1], Huimin Li[1], Tao Li[1], Pei Li[1], Wenting Zhao[1], Lingzhu Zi[1], Shiji Feng[1], Xuan Fan[1], Hailei Zhang[2], Dengfeng Peng[3,4,5,*], Feng Wang[6,7,*], Jianrong Qiu[8], Yanmin Yang[1,*]

[1]College of Physics Science and Technology, Hebei University, Baoding, 071002, China
[2]College of Chemistry & Materials Science, Hebei University, Baoding, 071002, China
[3]Shenzhen Key Laboratory of Intelligent Optical Measurement and Detection, Shenzhen University, Shenzhen, 518060, China
[4]Key Laboratory of Optoelectronic Devices and Systems of Ministry of Education and Guangdong Province, College of Physics and Optoelectronic Engineering, Shenzhen University, Shenzhen, 518060, China
[5]State Key Laboratory of Radio Frequency Heterogeneous Integration, Shenzhen University, Shenzhen, 518060, China
[6]Department of Materials Science and Engineering, City University of Hong Kong, 83 Tat Chee Avenue, Hong Kong SAR, China
[7]Hong Kong Institute for Clean Energy, City University of Hong Kong, 83 Tat Chee Avenue, Hong Kong SAR, China
[8]State Key Laboratory of Modern Optical Instrumentation, College of Optical Science and Engineering, Zhejiang University, Hangzhou, 310027, China

Corresponding authors:
lpl@hbu.edu.cn (L. Li);
pengdengfeng@szu.edu.cn (D. Peng);
fwang24@cityu.edu.hk (F. Wang);
yangym@hbu.edu.cn (Y. Yang).

Supplementary information file includes:

- **Supplementary Figs. 1 to 51;**
- **Supplementary Tables 1 to 4;**
- **Supplementary Notes 1 and 2;**
- **Supplementary references.**

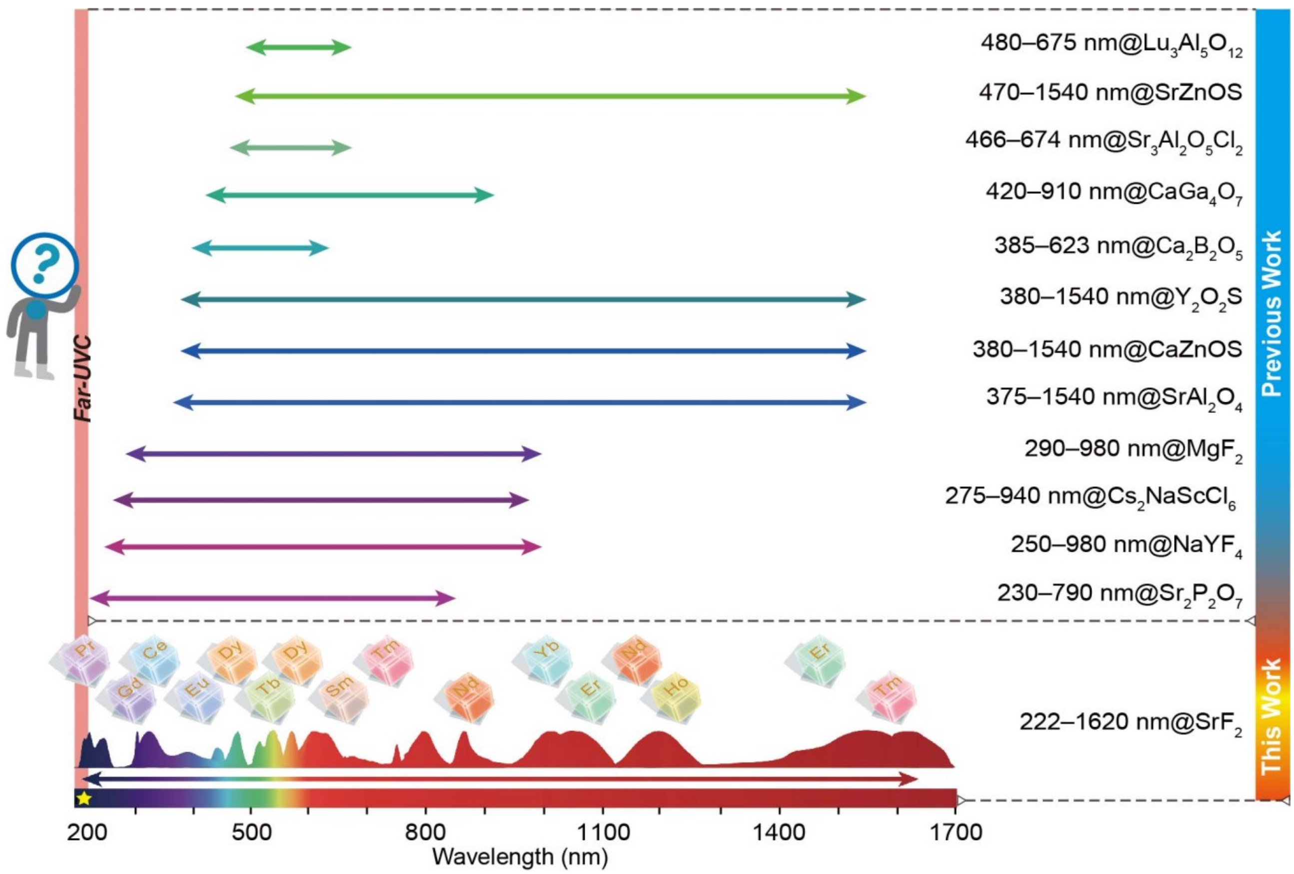

Supplementary Fig. 1 | Comparison of mechanoluminescence spectral coverage of different systems.

Supplementary Table 1 | Comparison of mechanoluminescence spectral coverage of SrF_2 doped with different lanthanides to previously reported systems.

Host matrix	Doped ions	Emission band (nm)	References
CaZnOS	Mn^{2+}, Cu^{+}, Bi^{3+}, Sb^{3+}, Ce^{3+}, Pr^{3+}, Nd^{3+}, Sm^{3+}, Eu^{3+}, Tb^{3+}, Dy^{3+}, Ho^{3+}, Er^{3+}, Tm^{3+}, Yb^{3+}	380–1540	[1, 2, 3, 4, 5, 6]
SrZnOS	Mn^{2+}, Pr^{3+}, Nd^{3+}, Sm^{3+}, Tb^{3+}, Dy^{3+}, Ho^{3+}, Er^{3+}, Tm^{3+}, Yb^{3+}	420–1540	[7]
Y_2O_2S	Pr^{3+}, Nd^{3+}, Sm^{3+}, Tb^{3+}, Dy^{3+}, Ho^{3+}, Er^{3+}, Tm^{3+}, Yb^{3+}	480–1540	[8, 9]
Lu_2O_2S	Eu^{3+}	580–705	[8]
La_2O_2S	Eu^{3+}	580–705	[8]
Gd_2O_2S	Eu^{3+}	615–705	[8]
(Zn,Cd)S	Mn^{2+}, Ag^{+}, Au^{+}, Cu^{2+}	430–620	[10]
BaZnOS	Mn^{2+}, Bi^{3+}	480–630	[11, 12]
ZnS	Cu^{2+}, Mn^{2+}, Mn^{2+}/Te^{2+}	456–648	[13, 14, 15, 16]
MgF_2	Mn^{2+}, Tm^{3+}, Yb^{3+}/Yb^{2+}, Dy^{3+}, Tb^{3+}, Eu^{3+}/Eu^{2+}, Sm^{3+}, Er^{3+}, Ho^{3+}	280–1000	[17, 18, 19, 20]
$KMgF_3$	Tb^{3+}	494–621	[21]
CaF_2	Tb^{3+}, Sm^{3+}, Tm^{3+}, $Eu^{2+/3+}$	425–825	[22, 23]
$NaYF_4$	Pr^{3+}, Sm^{3+}, Tb^{3+}, Dy^{3+}, Ho^{3+}, Er^{3+}, Tm^{3+}	250–980	[24, 25, 26]
$NaLuF_4$	Tb^{3+}, Ho^{3+}	486–647	[27, 28]
ZnF_2/ZnO	Mn^{2+}	585	[29]
$NaCa_2GeO_4F$	Mn^{2+}	570	[30]
$Sr_3(Al,Ga)O_4F$	Eu^{3+}, Tb^{3+}	488–704	[31]
Cs_2ZrCl_6	Te^{4+}	576	[32]
$CaCl_2$	Eu^{2+}	432	[33]
(Na,K)Cl	crystal	Not mentioned	[34]
$Sr_5(PO_4)_3Cl$	Eu^{2+}	455	[35]
$Sr_3Al_2O_5Cl_2$	Dy^{3+}, Eu^{2+}, Tb^{3+}, Ce^{3+}, Tm^{3+}/Eu^{3+}	466–674	[36, 37, 38]
$Sr_5(PO_4)_3(F,Cl,Br)$	Eu^{3+}/Eu^{2+}	446–700	[39]
$Sr_5(PO_4)_3Cl$	Eu^{2+}, Eu^{2+}/Mn^{2+}	400–700	[40]
$Cs_2NaScCl_6$	Sb^{3+}, Pr^{3+}, Nd^{3+}, Sm^{3+}, Tb^{3+}, Dy^{3+}, Ho^{3+}, Er^{3+}, Tm^{3+}, Yb^{3+}, Gd^{3+}, Ce^{3+}, Ag^{+}/Bi^{3+}, Mn^{2+}	275–940	[41]
Cs_2HfCl_6	Te^{4+}	557	[42]
$Ca_6BaP_4O_{17}$	Ce^{3+}	488	[43]
$Ca_9Bi(PO_4)_7$	Ce^{3+}, Bi^{2+}	356–682	[44]
$SrMg_2(PO_4)_2$	Eu^{2+}	412	[45, 46, 47]
$CaZr(PO_4)_2$	Eu^{2+}	474	[48, 49, 50]

$Sr_8MgCe(PO_4)_7$	Ce^{3+}, Tb^{3+}, Mn^{2+}	373–620	[51]
$Ca_6BaP_4O_{17}$	Eu^{2+}	540	[52]
$Ca_9Al(PO_4)_7$	Tb^{3+}, Mn^{2+}	480–648	[53]
$Sr_2P_2O_7$	Pr^{3+}, Tb^{3+}, Dy^{3+}, Sm^{3+}, Eu^{2+}, Ce^{3+}, Sn^{2+}, Mn^{2+}	230–800	[54, 55]
$Ca_9Al(PO_4)_7$	Ce^{3+}	344–700	[56]
$Ca_9NaMg(PO_4)_7$	Tb^{3+}	370–624	[57]
$SrAl_2O_4$	Eu^{2+}/Dy^{3+}, Ce^{3+}/Ho^{3+}, Eu^{2+}/Er^{3+}, $Eu^{2+}/Cr^{3+}/Nd^{3+}$, Ce^{3+}, Eu^{2+}, Nd^{3+}/Eu^{2+}, Er^{3+}/Eu^{2+}, Ce^{3+}/Ho^{3+}	375–1540	[58]
$LaAlO_3$	Cr^{3+}	685–750	[59]
$Lu_3Al_5O_{12}$	Ce^{3+}, Pr^{3+}, Eu^{3+}, Tb^{3+}, Sm^{3+}, Ho^{3+}, Dy^{3+}, Er^{3+}, Nd^{3+}, Tm^{3+}	480–725	[60]
$Y_3Al_5O_{12}$	Ce^{3+}, Cr^{3+}	560–688	[61, 62]
$CaYAl_3O_7$	Eu^{2+}, Ce^{3+}	421–445	[63, 64]
$ZnAl_2O_4$	Mn^{2+}	512	[65]
$SrMgAl_{10}O_{17}$	Ce^{3+}	400–480	[66]
$SrMgAl_6O_{11}$	Eu^{2+}	512	[67]
$BaMgAl_{12}O_{17}$	Eu^{2+}	450	[68]
$CaLaAl_3O_7$	Tb^{3+}	413–622	[69]
$BaLaAl_3O_7$	Eu^{3+}	595–615	[70]
$CaGa_4O_7$	Pr^{3+}, Tb^{3+}, Er^{3+}, Dy^{3+}, Mn^{2+}, Sm^{3+}, Eu^{3+}, Tm^{3+}, Nd^{3+}	420–910	[71, 72]
$Ca_5Ga_6O_{14}$	Tb^{3+}	484–625	[73]
$Y_3Ga_5O_{12}$	Tb^{3+}	380–690	[74]
$MgGa_2O_4$	Mn^{2+}, Cr^{3+}, Bi^{3+}	480–710	[75, 76, 77,]
$CaGa_2O_4$	Pr^{3+}/Li^{+}	485–651	[78]
$Ca_3Ga_4O_9$	Tb^{3+}, Eu^{3+}	380–701	[79, 80]
$SrGa_{12}O_{19}$	Cr^{3+}, Cr^{3+}/Pr^{3+}	710–750	[81, 82, 83]
$Y_3Al_2Ga_3O_{12}$	Gd^{3+}	310	[84]
$Lu_3Al_2Ga_3O_{12}$	Cr^{3+}, Tb^{3+}	380–720	[85, 86]
$Y_3Al_3Ga_2O_{12}$	Ce^{3+}	528	[87]
$CaSrGa_4O_8$	Tb^{3+}	480–630	[88]
Y_3GaO_6	Tb^{3+}	484–625	[89]
$LiGa_5O_8$	Matrix, Cr^{3+}, Pr^{3+}	525–716	[81, 90, 91]
$LiGaO_2$	Fe^{3+}, Mn^{2+}	660–746	[92, 93]
$ZnGa_2O_4$	Mn^{2+}, Cr^{3+}	505–692	[75, 94]
$Lu_3Al_2Ga_3O_{12}$	Tb^{3+}, Eu^{3+}	383–709	[95]
$(Li,Na)_2(Zn,Mg)GeO_4$	Mn^{2+}	515–535	[96]
$Zn_3Ga_2GeO_8$	Cr^{3+}	700	[81]

$CaZnGe_2O_6$	Mn^{2+}	676	97, 98
$Ca_2YGa_3Ge_2O_{12}$	Cr^{3+}, Cr^{3+}/Nd^{3+}	767–1340	99
$Mg_3Ga_2GeO_8$	Cr^{3+}	740–801	100
$MgGeO_3$	Mn^{2+}	691	101
$CaMgGe_2O_6$	Mn^{2+}	670	102
$Zn_2(Ge_{0.9}Si_{0.1})O_4$	Mn^{2+}	535	103
Na_2ZnSiO_4	Mn^{2+}	514	96
$Sr_2MgSi_2O_7$	Eu^{2+}/Dy^{3+}, Eu^{2+}	470–580	104, 105
$Ca_2MgSi_2O_7$	Eu^{2+}	545	106
$Ca_2Al_2SiO_7$	Ce^{3+}	400	107
$Sr(Ba,Ca,Sr)MgSi_2O_7$	Eu^{2+}	450–490	108
$(Ca,Sr)Al_2Si_2O_8$	Eu^{2+}	403–428	109
$(Ca,Sr)_8Mg_3Al_2Si_7O_{28}$	Ce^{3+}	395–405	110
$Ca_2Ga_2SiO_7$	Tb^{3+}	495–620	111
$Y_3Ga_3MgSiO_{12}$	Cr^{3+}	731–780	112
$CaNb_2O_6$	Pr^{3+}	613	113
$Ca_2Nb_2O_7$	Pr^{3+}	613	113
$Ca_3Nb_2O_8$	Pr^{3+}	613	113
$Sr_2Nb_2O_7$	Pr^{3+}	red	114
$NaNbO_3$	Pr^{3+}/Er^{3+}	613	115
$LiNbO_3$	Pr^{3+}, Nd^{3+}	619–895	116, 117
$(Na,Mg)NbO_3$	Pr^{3+}	605	118
$LiTaO_3$	Tb^{3+}, Pr^{3+}/Gd^{3+}	480–625	119, 120
$(Ba,Ca)TiO_3$	Pr^{3+}	620	121, 122, 123
$Sr_3Sn_2O_7$	Sm^{3+}, Nd^{3+}, Nd^{3+}/Yb^{3+}	570–1350	124, 125, 126, 127, 128, 129, 130
Sr_2SnO_4	Sm^{3+}	574–745	131
$SrZn_2S_2O$	Mn^{2+}	610	132
ZrO_2	Sm^{3+}/Nd^{3+}, Ti^{4+}	478–660	133, 134
Ga_2O_3	Cr^{3+}/In^{3+}	715–830	135
$BaSi_2O_2N_2$	Eu^{2+}	500	8
$Ba_{0.5}Sr_{0.5}Si_2O_2N_2$	Eu^{2+}	505	61
B_2O_3-SiO_2-ZnO	Tb^{3+}, Tm^{3+}, Eu^{3+}	455–710	136
$Ca_2B_2O_5$	Tb^{3+}, Dy^{3+}, Sm^{3+}, Eu^{3+}, Ce^{3+}	350–800	137
$(Ca,Sr,Ba)_2(Ga,Ln,Sc,Y)SbO_6$	Cr^{3+}	825–1010	138
$BaSi_2O_2N_2$	Eu^{2+}	498	139
ZnB_2O_4	Mn^{2+}	550	140

Supplementary Table 2 | Comparison of radius of different lanthanides and Sr^{2+} in an octahedral coordination environment.

Ion	Ion radius (pm)
Sr^{2+}	126
Ce^{3+}	114.3
Pr^{3+}	112.6
Nd^{3+}	110.9
Sm^{3+}	107.9
Eu^{2+}	125
Eu^{3+}	106.6
Gd^{3+}	105.3
Tb^{3+}	104.0
Dy^{3+}	102.7
Ho^{3+}	101.5
Er^{3+}	100.4
Tm^{3+}	99.4
Yb^{3+}	98.5

Supplementary Table 3 | Structural information of $SrF_2:Pr^{3+}$ determined by the refinement results.

	$SrF_2:Pr^{3+}$
Space group	*Fm*–3*m*
R_p	9.96
R_{wp}	13.72
χ^2	2.336
a (Å)	5.7986
b (Å)	5.7986
c (Å)	5.7986
$\alpha=\beta=\gamma$	90.000°

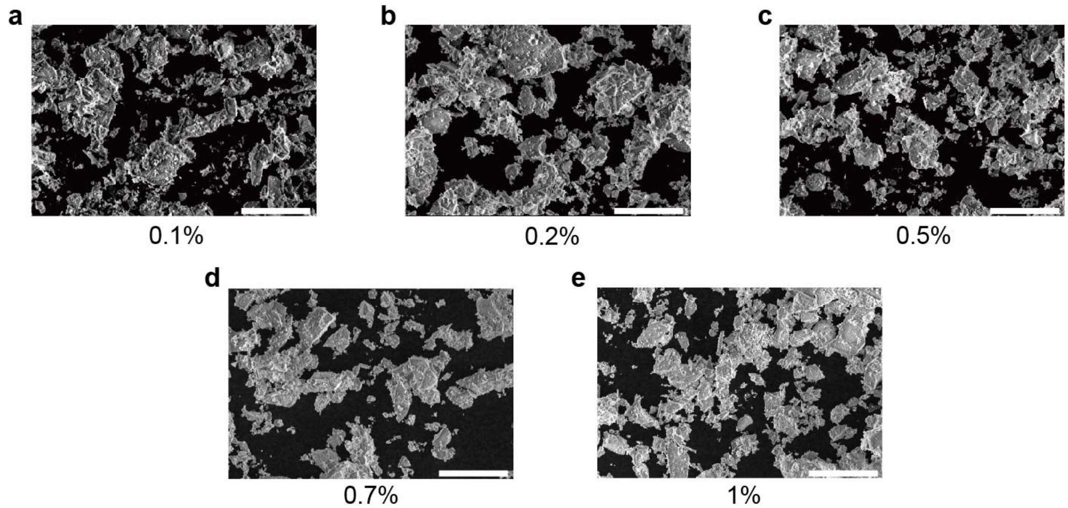

Supplementary Fig. 2 | Scanning electron microscopy images of SrF_2 doped with different concentrations. **a** SrF_2:0.1%Pr^{3+}, **b** SrF_2:0.2%Pr^{3+}, **c** SrF_2:0.5%Pr^{3+}, **d** SrF_2:0.7%Pr^{3+}, and **e** SrF_2:1%Pr^{3+}. Scale bar: 50 μm.

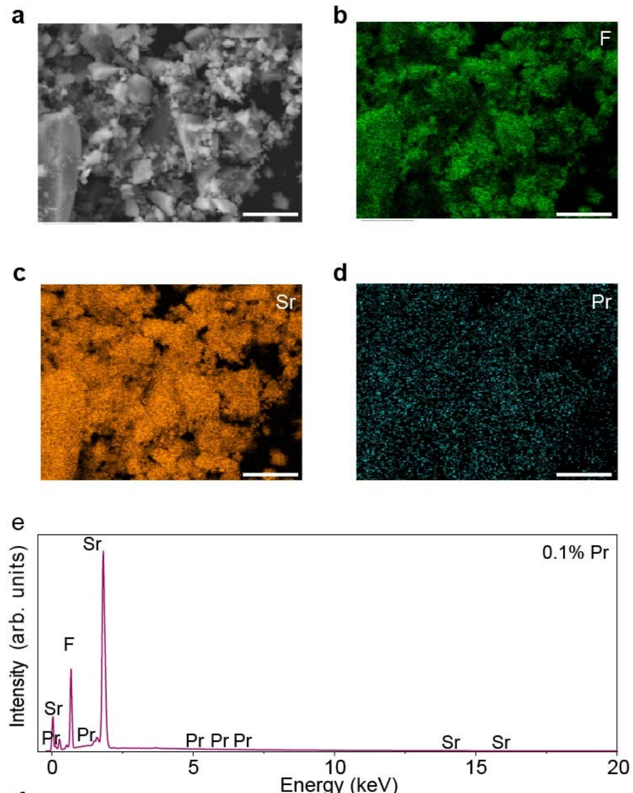

f

Element	Signal type	Weight %	Atomic %	Error % (Weight %)
F	EDS	29.79	66.19	0.12
Sr	EDS	70.10	33.77	0.14
Pr	EDS	0.11	0.03	0.12

Supplementary Fig. 3 | Elemental analysis of SrF_2:0.1%Pr^{3+}. a Scanning electron microscopy image, **b** F, **c** Sr, and **d** Pr elemental mappings, **e** Energy dispersive spectroscopy spectrum and **f** Elemental analysis data of SrF_2:0.1%Pr^{3+}. Scale bar: 50 µm.

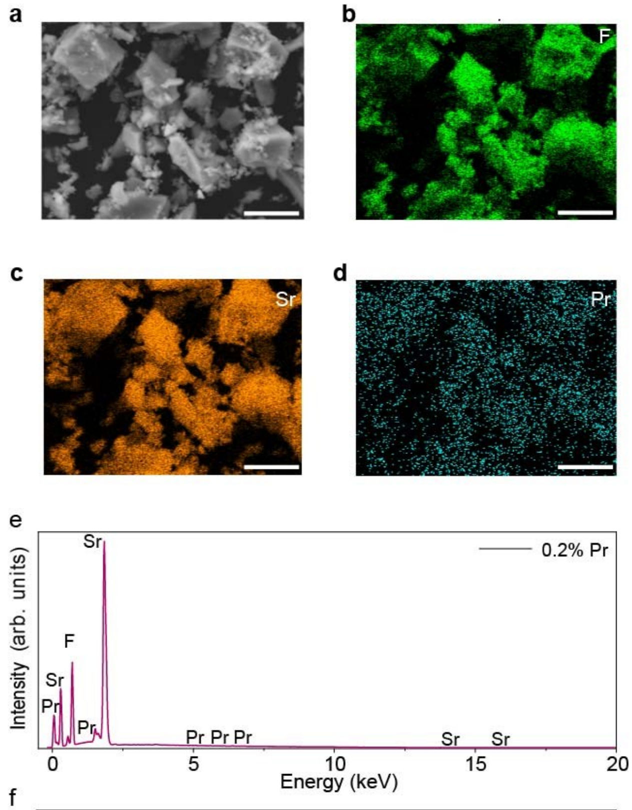

f

Element	Signal type	Weight %	Atomic %	Error % (Weight %)
F	EDS	29.75	66.16	0.15
Sr	EDS	70.02	33.77	0.18
Pr	EDS	0.23	0.07	0.17

Supplementary Fig. 4 | Elemental analysis of SrF_2:0.2%Pr^{3+}. a Scanning electron microscopy image, **b** F, **c** Sr, and **d** Pr elemental mappings, **e** Energy dispersive spectroscopy spectrum and **f** Elemental analysis data of SrF_2:0.2%Pr^{3+}. Scale bar: 50 μm.

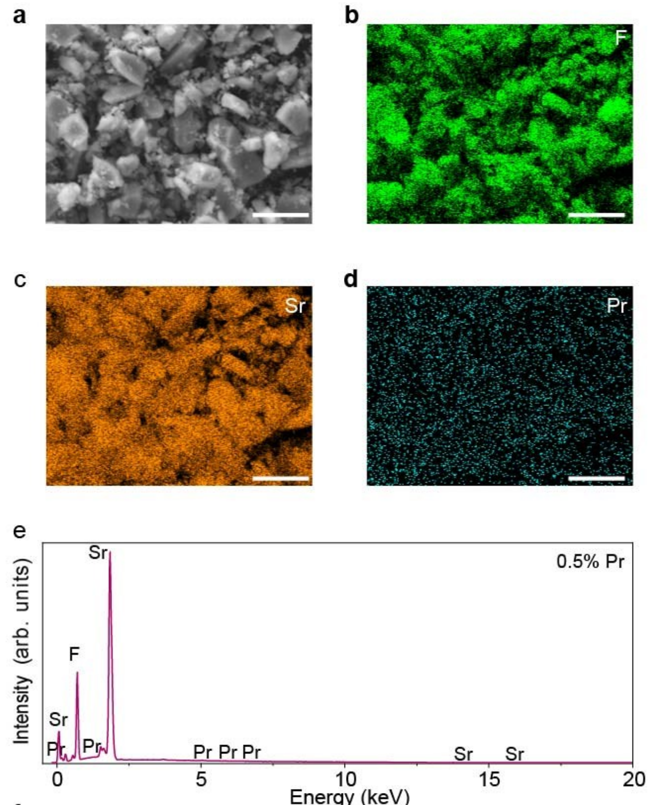

f

Element	Signal type	Weight %	Atomic %	Error % (Weight %)
F	EDS	30.43	66.93	0.14
Sr	EDS	69.01	32.91	0.17
Pr	EDS	0.56	0.16	0.15

Supplementary Fig. 5 | Elemental analysis of SrF_2:0.5%Pr^{3+}. a Scanning electron microscopy image, **b** F, **c** Sr, and **d** Pr elemental mappings, **e** Energy dispersive spectroscopy spectrum and **f** Elemental analysis data of SrF_2:0.5%Pr^{3+}. Scale bar: 50 μm.

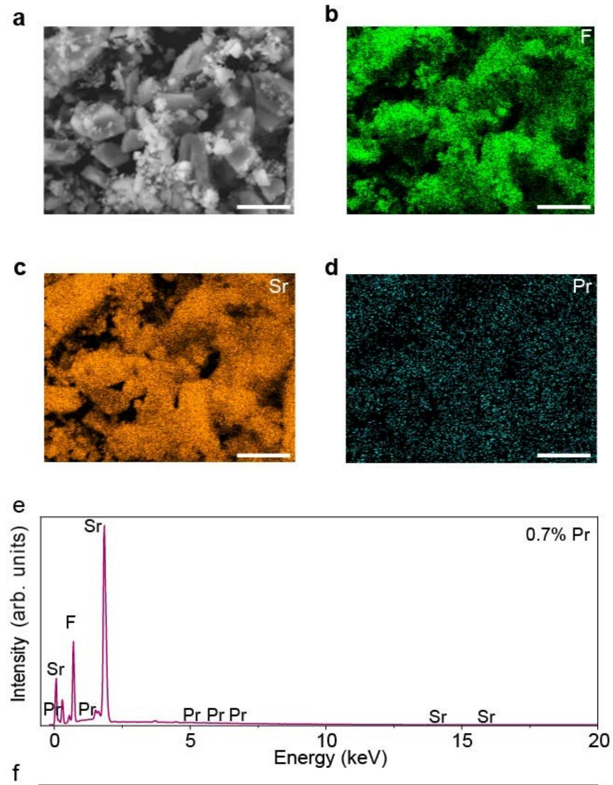

f

Element	Signal type	Weight %	Atomic %	Error % (Weight %)
F	EDS	30.02	66.52	0.12
Sr	EDS	69.19	33.24	0.15
Pr	EDS	0.79	0.24	0.14

Supplementary Fig. 6 | Elemental analysis of SrF_2:0.7%Pr^{3+}. a Scanning electron microscopy image, **b** F, **c** Sr, and **d** Pr elemental mappings, **e** Energy dispersive spectroscopy spectrum and **f** Elemental analysis data of SrF_2:0.7%Pr^{3+}. Scale bar: 50 µm.

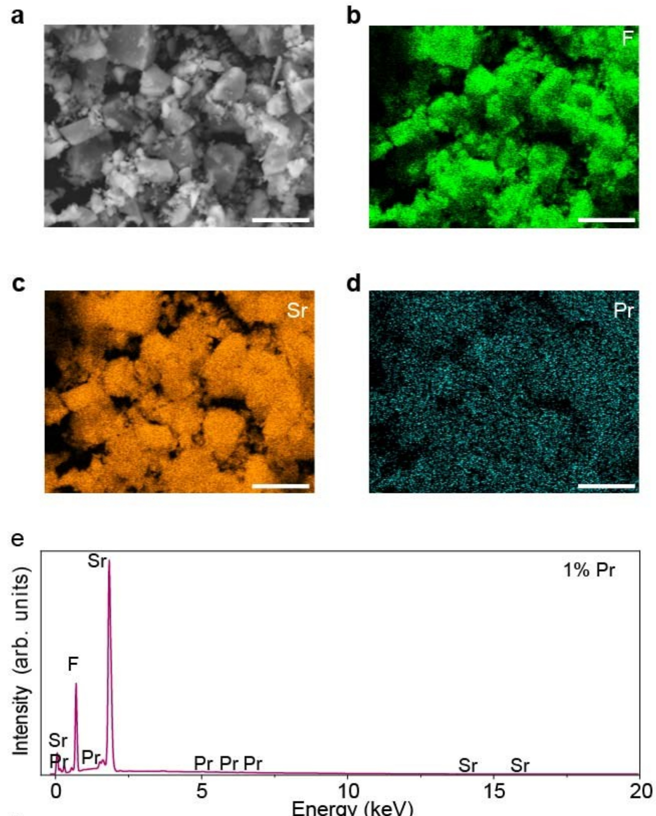

f

Element	Signal type	Weight %	Atomic %	Error % (Weight %)
F	EDS	29.47	65.97	0.08
Sr	EDS	69.39	33.68	0.09
Pr	EDS	1.14	0.34	0.08

Supplementary Fig. 7 | Elemental analysis of SrF_2:1%Pr^{3+}. a Scanning electron microscopy image, **b** F, **c** Sr, and **d** Pr elemental mappings, **e** Energy dispersive spectroscopy spectrum and **f** Elemental analysis data of SrF_2:1%Pr^{3+}. Scale bar: 50 μm.

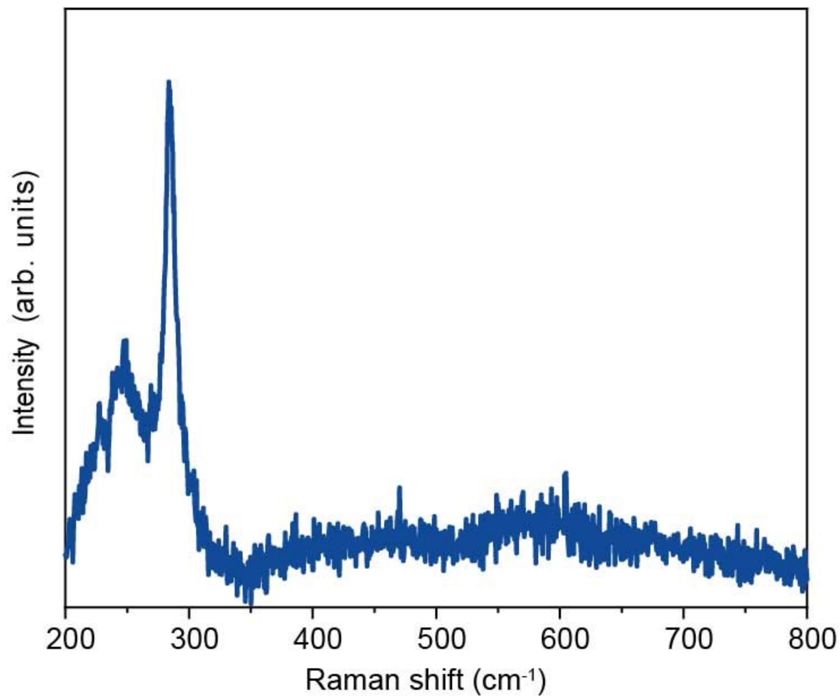

Supplementary Fig. 8 | Raman spectrum of SrF_2:0.5%Pr^{3+}.

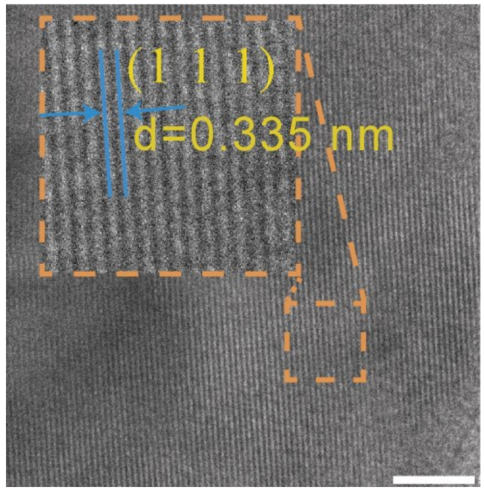

Supplementary Fig. 9 | High-resolution transmission electron microscopy image of SrF_2:0.5%Pr^{3+} (Scale bar: 5 nm).

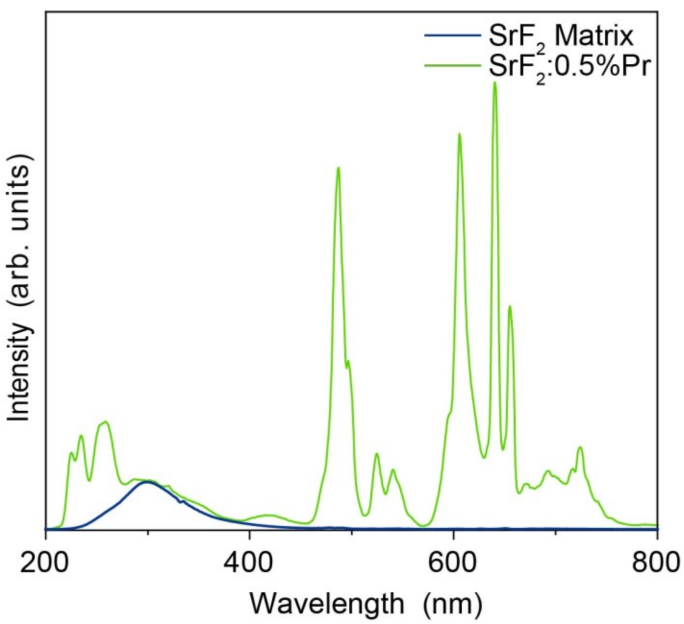

Supplementary Fig. 10 | Comparison of photoluminescence spectra between SrF_2:0.5%Pr^{3+} and SrF_2 matrix. The broadband peak at 300 nm is attributed to the luminescence from the self-trapped exciton of the host.

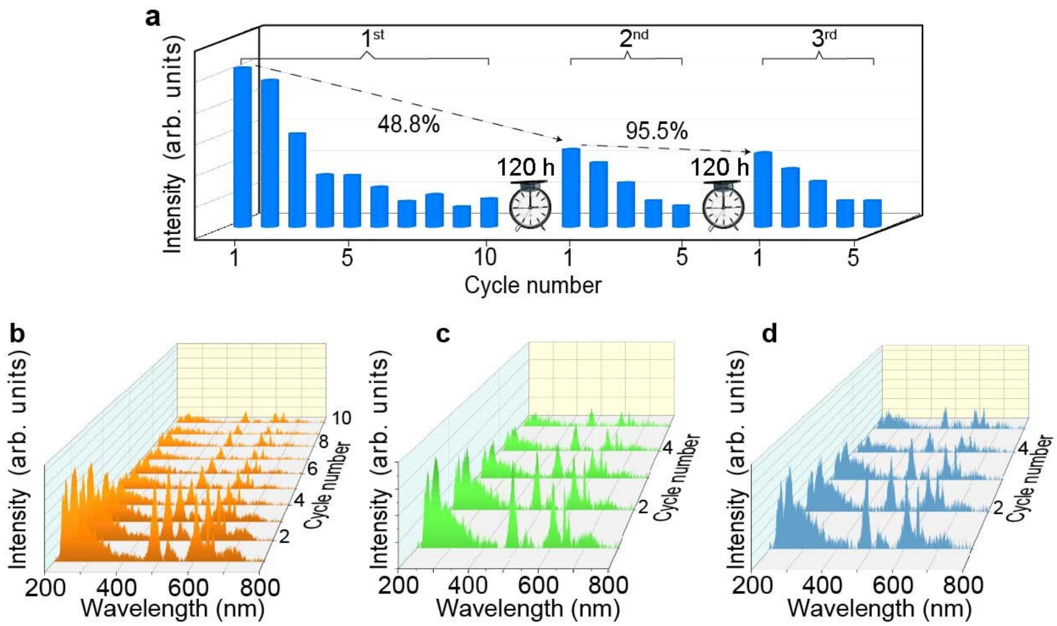

Supplementary Fig. 11 | Repeatability test of self-recoverable mechanoluminescence of SrF_2:0.5%Pr^{3+} before X-ray charging. a Repeatability test results of self-recoverable mechanoluminescence intensity. Original ML spectra collected during the **b** First, **c** Second and **d** Third cycles.

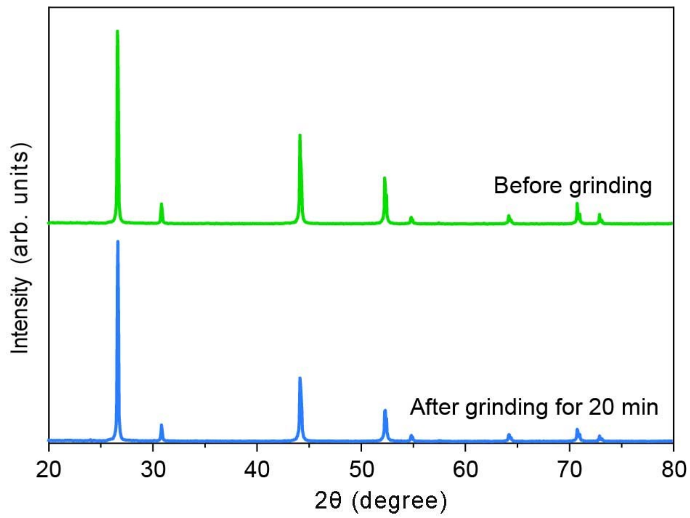

Supplementary Fig. 12 | X-ray diffraction patterns of SrF_2:0.5%Pr^{3+} before and after grinding for 20 min.

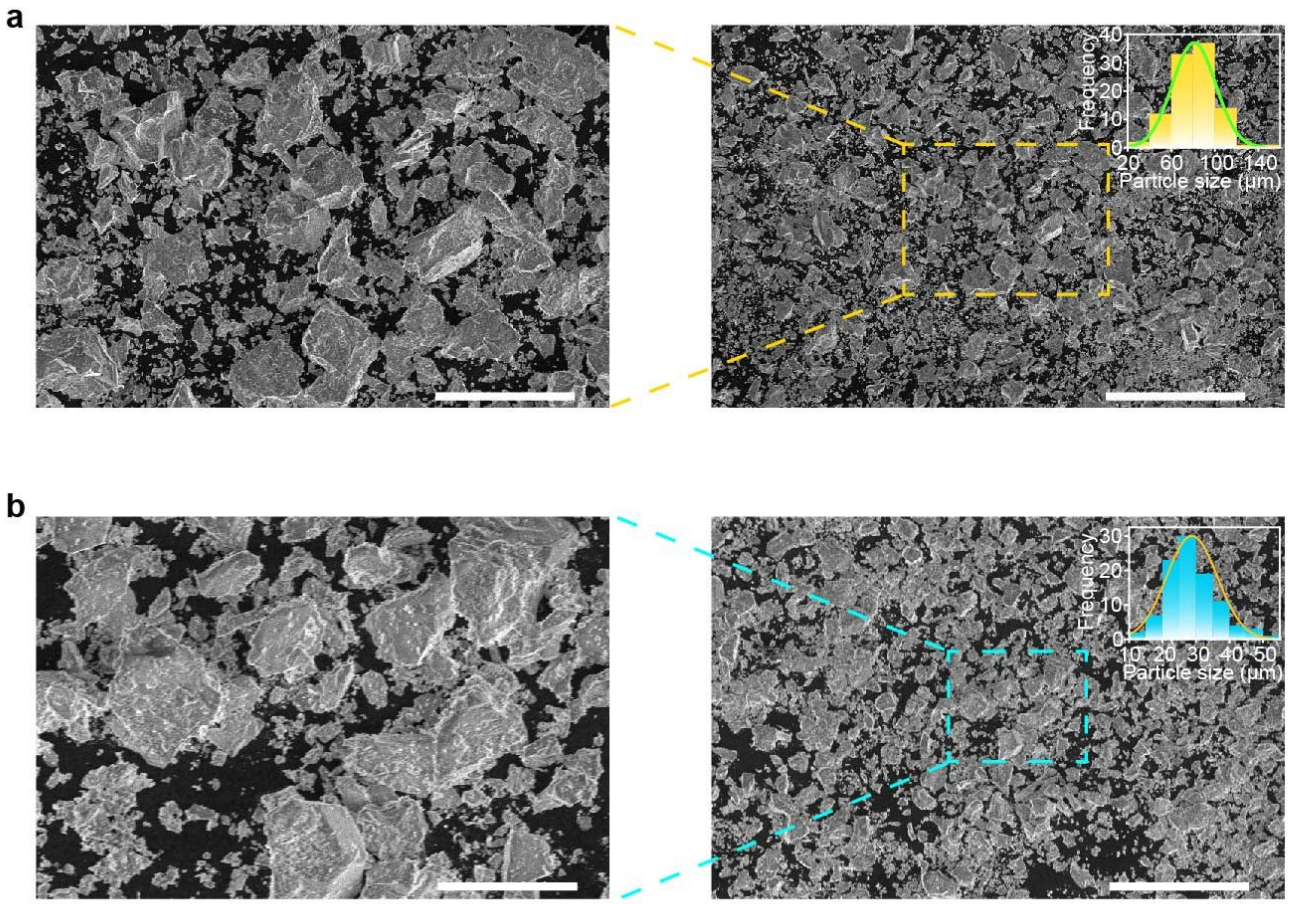

Supplementary Fig. 13 | Comparison of particle size of SrF_2:0.5%Pr^{3+} before and after grinding. Scanning electron microscopy images of SrF_2:0.5%Pr^{3+}: **a** Before (Scale bar: 500 μm) and **b** After continuous grinding for 20 min (Scale bar: 200 μm).

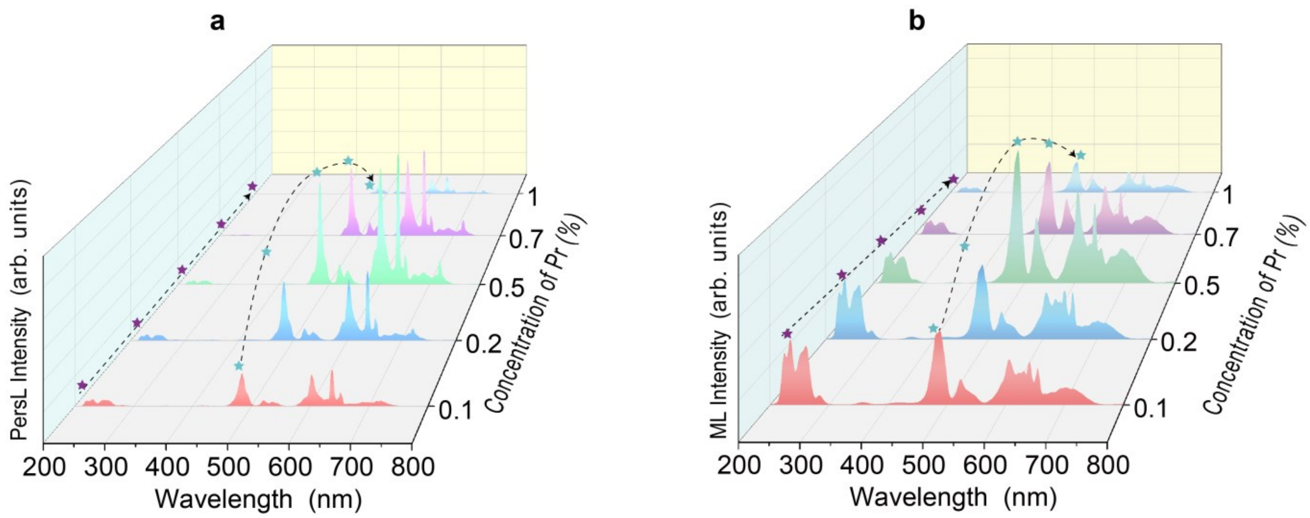

Supplementary Fig. 14 | Persistent luminescence (PersL) and mechanoluminescence (ML) spectra of SrF_2 doped with different concentration of Pr^{3+}. a PersL spectra and **b** ML spectra of SrF_2 doped with x%mol Pr^{3+} ($x = 0.1, 0.2, 0.5, 0.7$ and 1).

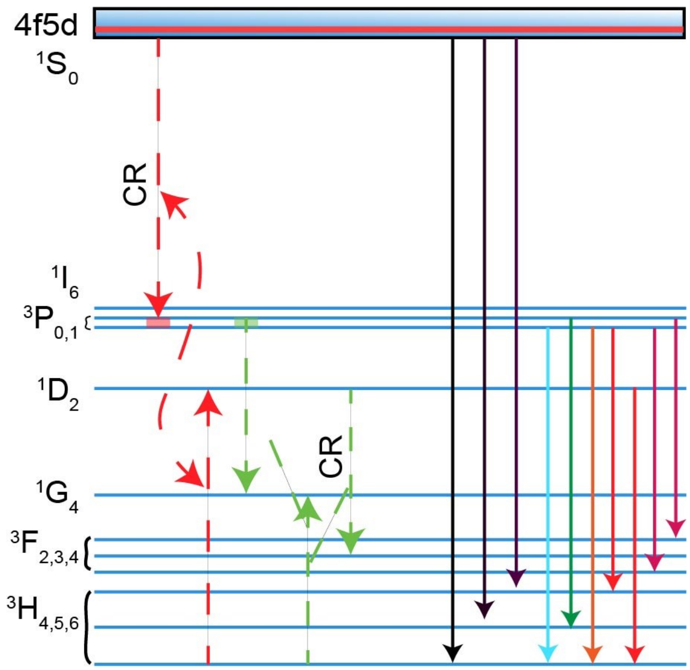

Supplementary Fig. 15 | Energy levels diagram of Pr^{3+} and possible cross-relaxation (CR) processes.

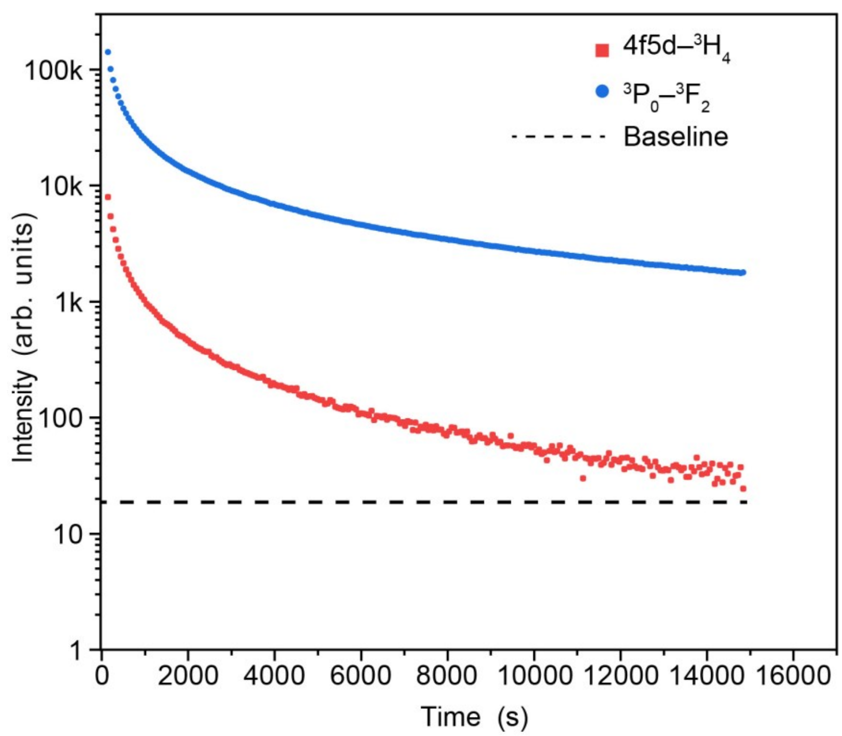

Supplementary Fig. 16 | Comparison of visible and UVC persistent luminescence (PersL) decay curves of SrF_2:0.5%Pr^{3+}. For the visible PersL decay curve, the $^3P_0 \rightarrow ^3F_2$ transition of Pr^{3+} was monitored. For the UVC PersL decay curve, the 4d5d$\rightarrow ^3H_4$ transition of Pr^{3+} was monitored. Before test, the sample of SrF_2:0.5%Pr^{3+} was subjected to X-ray irradiation for 5 min.

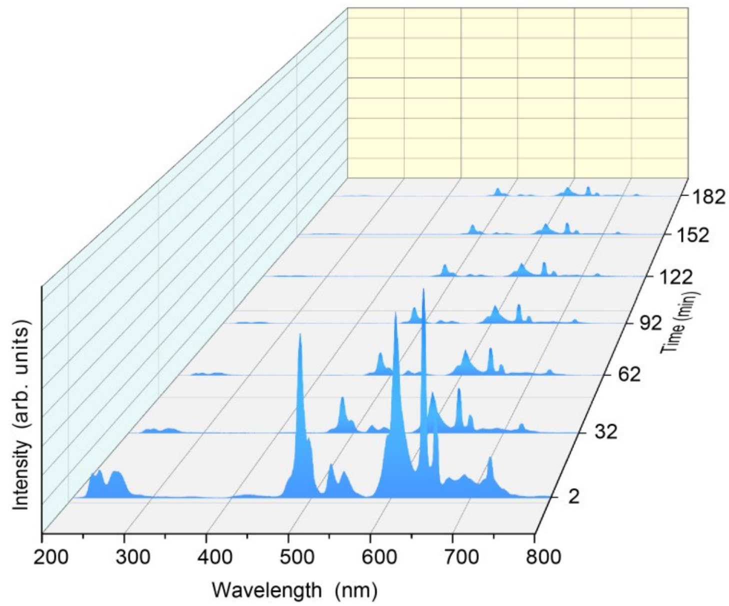

Supplementary Fig. 17 | Persistent luminescence spectra of SrF_2:0.5%Pr^{3+} following 5 min of X-ray irradiation.

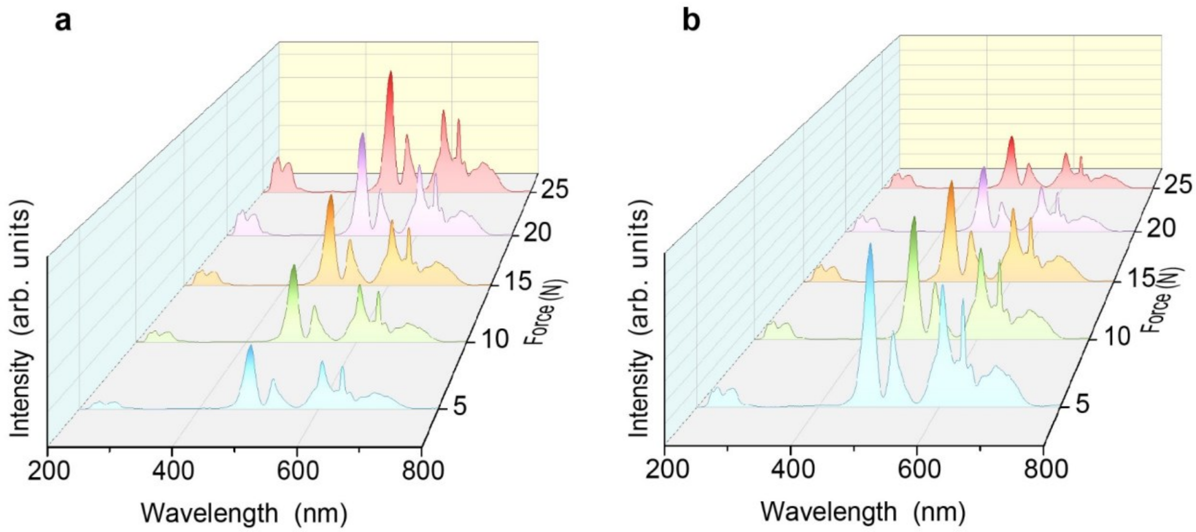

Supplementary Fig. 18 | Mechanoluminescence spectra under different forces. a Original and **b** Normalized mechanoluminescence spectra of SrF_2:0.5%Pr^{3+}.

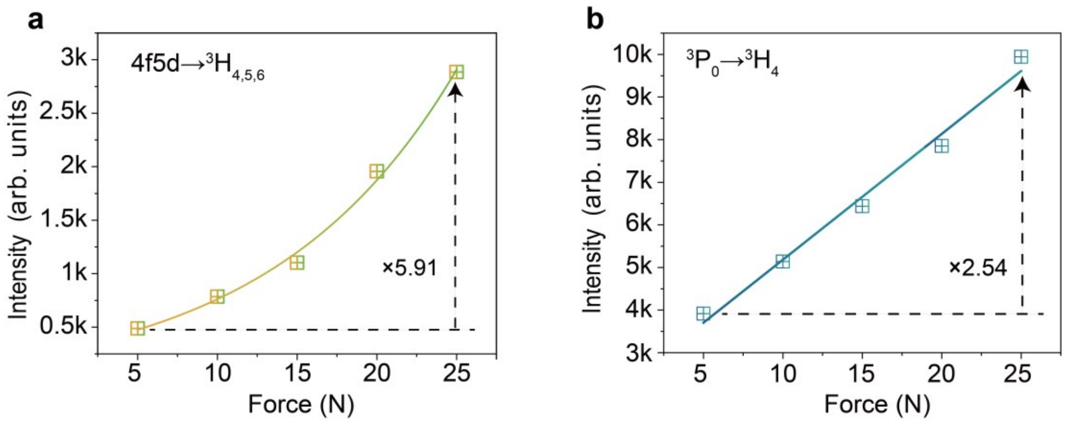

Supplementary Fig. 19 | Effect of force on mechanoluminescence intensity. Mechanoluminescence intensity of **a** 4f5d→$^3H_{4,5,6}$ and **b** $^3P_0$→$^3H_4$ transitions of Pr^{3+} of SrF_2:0.5%Pr^{3+} as a function of external force in the range of 5–25 N.

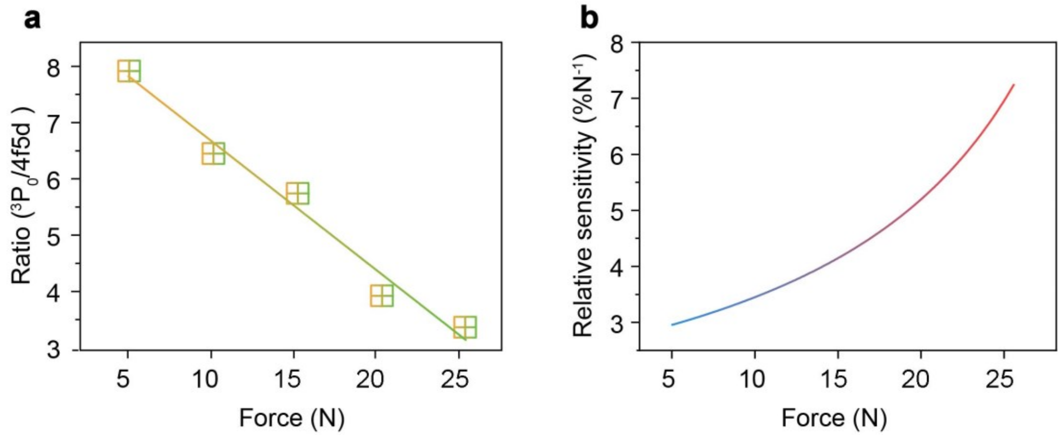

Supplementary Fig. 20 | Ratiometric stress sensing. a Mechanoluminescence intensity ratio between the $^3P_0 \rightarrow ^3H_4$ and 4f5d$\rightarrow ^3H_{4,5,6}$ transitions of Pr^{3+} of SrF_2:0.5%Pr^{3+}, and **b** Relative sensitivity of proposed ratiometric stress sensing method as a function of external force in the range of 5–25 N.

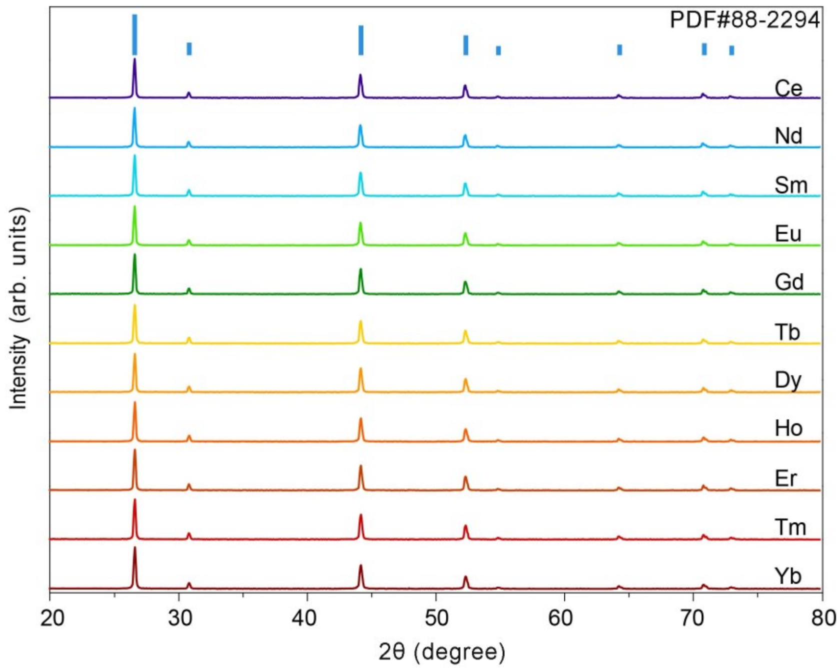

Supplementary Fig. 21 | X-ray diffraction patterns of SrF_2 doped with different lanthanides (0.5%mol).

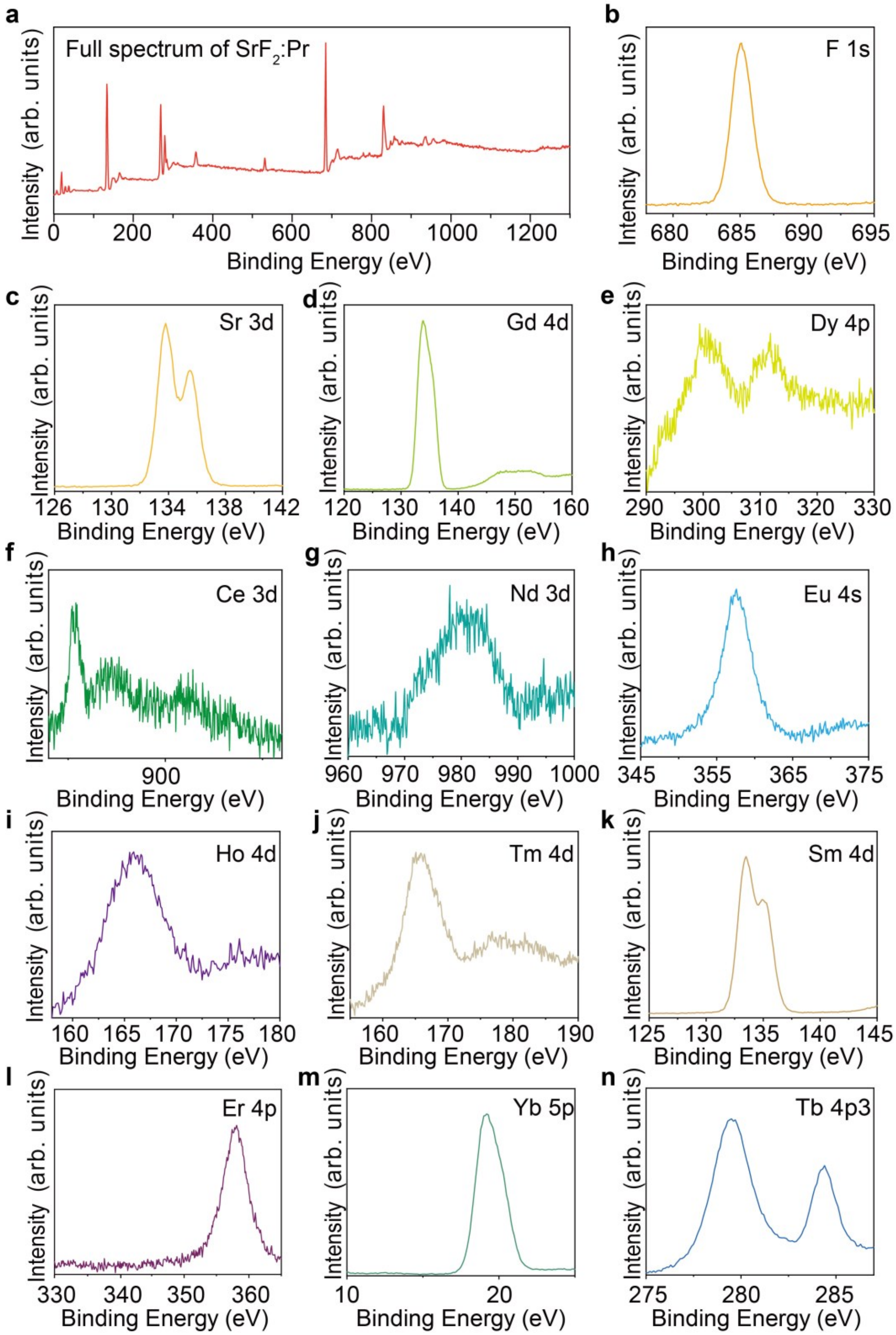

Supplementary Fig. 22 | X-ray photoelectron spectroscopy results of SrF_2 doped with different lanthanides (0.5%mol). **a** Full spectrum of SrF_2:Pr. **b–n** specific lanthanides: **b** F, **c** Sr, **d** Gd, **e** Dy, **f** Ce, **g** Nd, **h** Eu, **i** Ho, **j** Tm, **k** Sm, **l** Er, **m** Yb and **n** Tb.

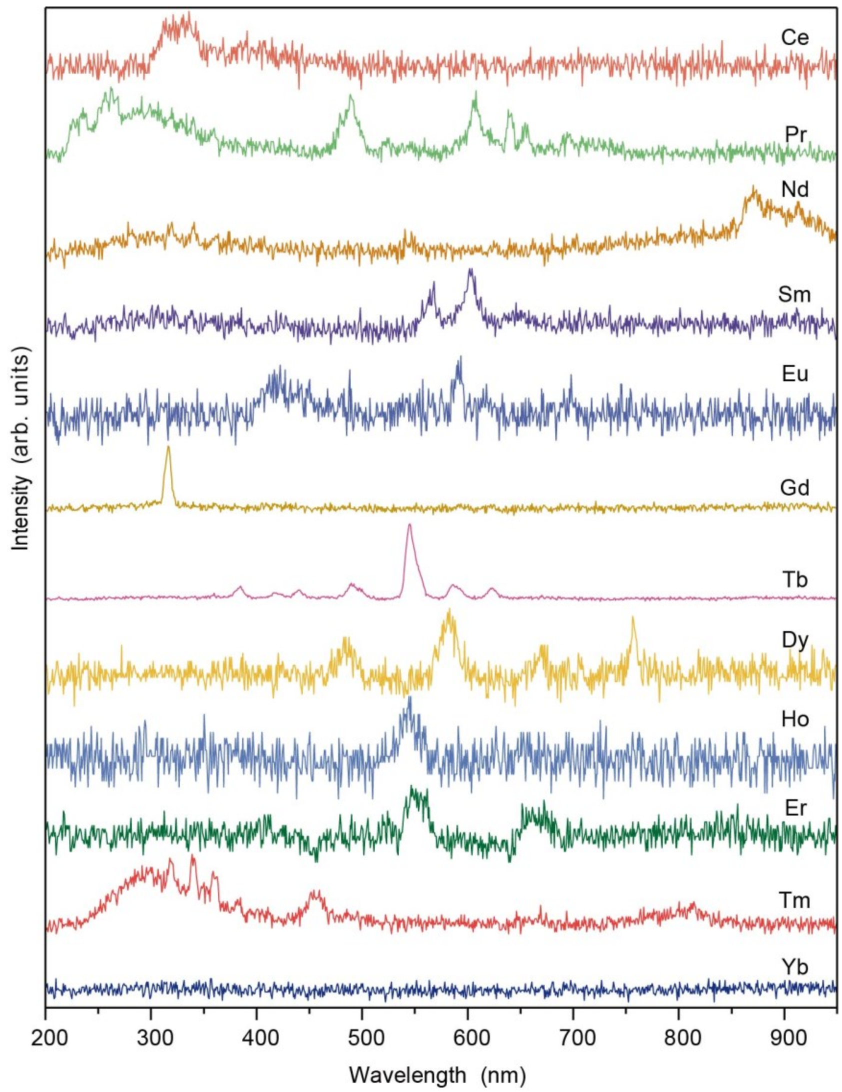

Supplementary Fig. 23 | Mechanoluminescence spectra of SrF_2 doped with different lanthanides (0.5%mol) before X-ray charging.

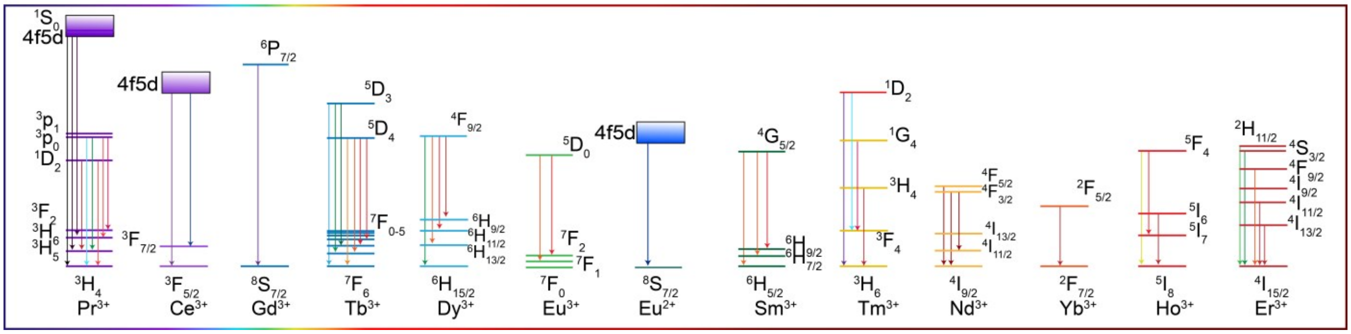

Supplementary Fig. 24 | Energy level diagrams of Pr^{3+}, Ce^{3+}, Gd^{3+}, Tb^{3+}, Dy^{3+}, $Eu^{2+,3+}$, Sm^{3+}, Tm^{3+}, Nd^{3+}, Yb^{3+}, Ho^{3+} and Er^{3+}.

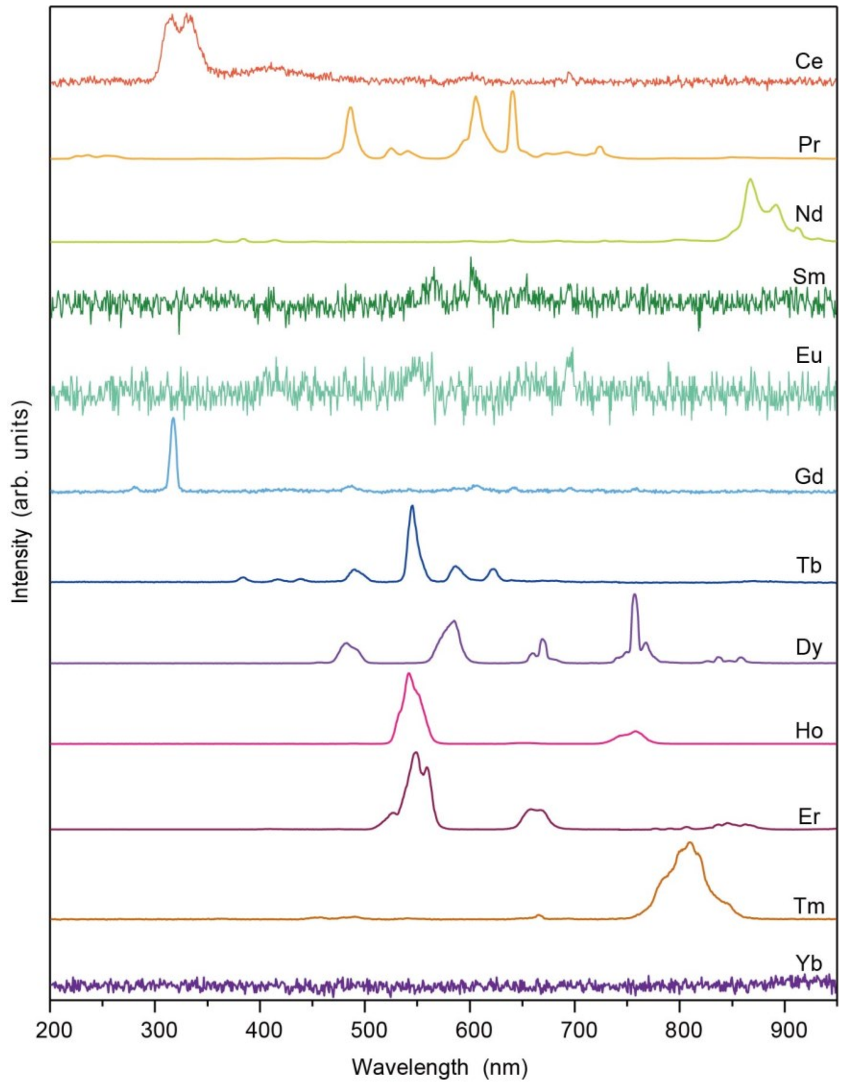

Supplementary Fig. 25 | Persistent luminescence spectra of SrF_2 doped with different lanthanides (0.5%mol) after X-ray irradiation over the 200–950 nm range.

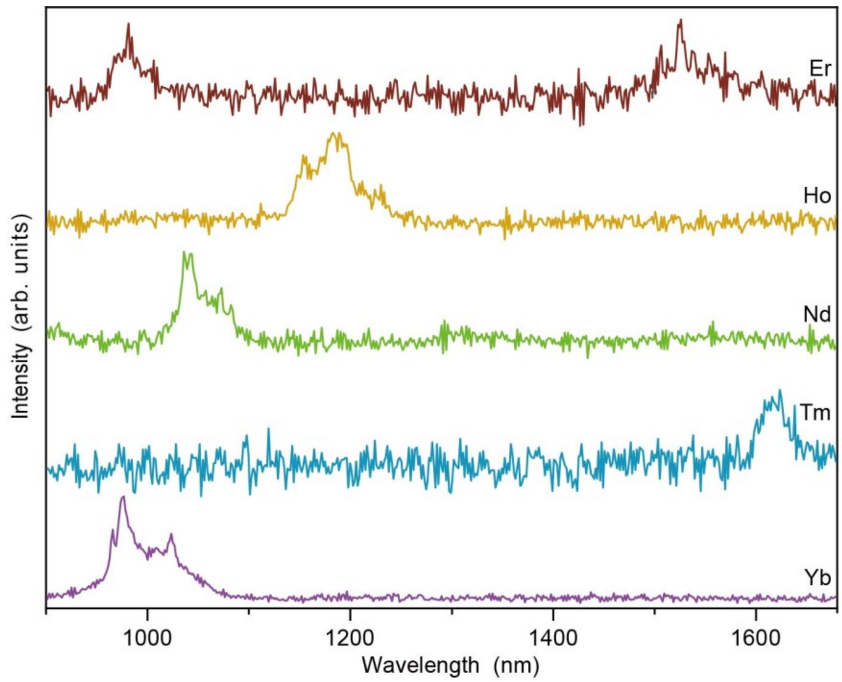

Supplementary Fig. 26 | Persistent luminescence spectra of SrF_2 doped with different lanthanides (0.5%mol) after X-ray irradiation over the 900–1680 nm range.

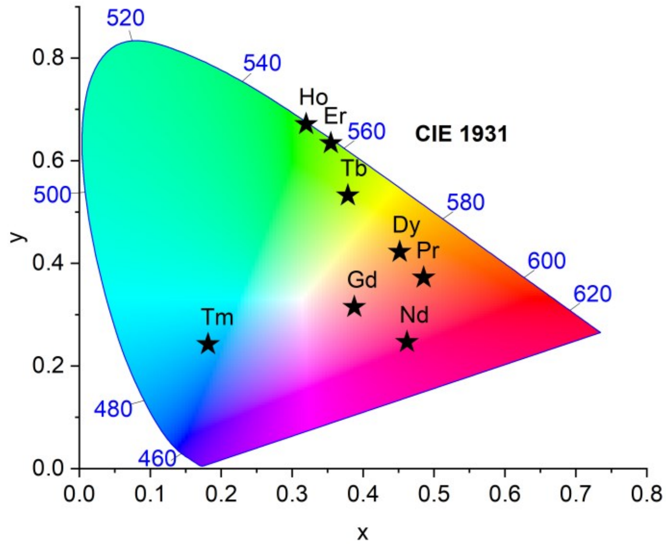

Supplementary Fig. 27 | Commission Internationale de l'Éclairage (CIE) chromatic coordinates of persistent luminescence from SrF_2 doped with different lanthanides (0.5%mol).

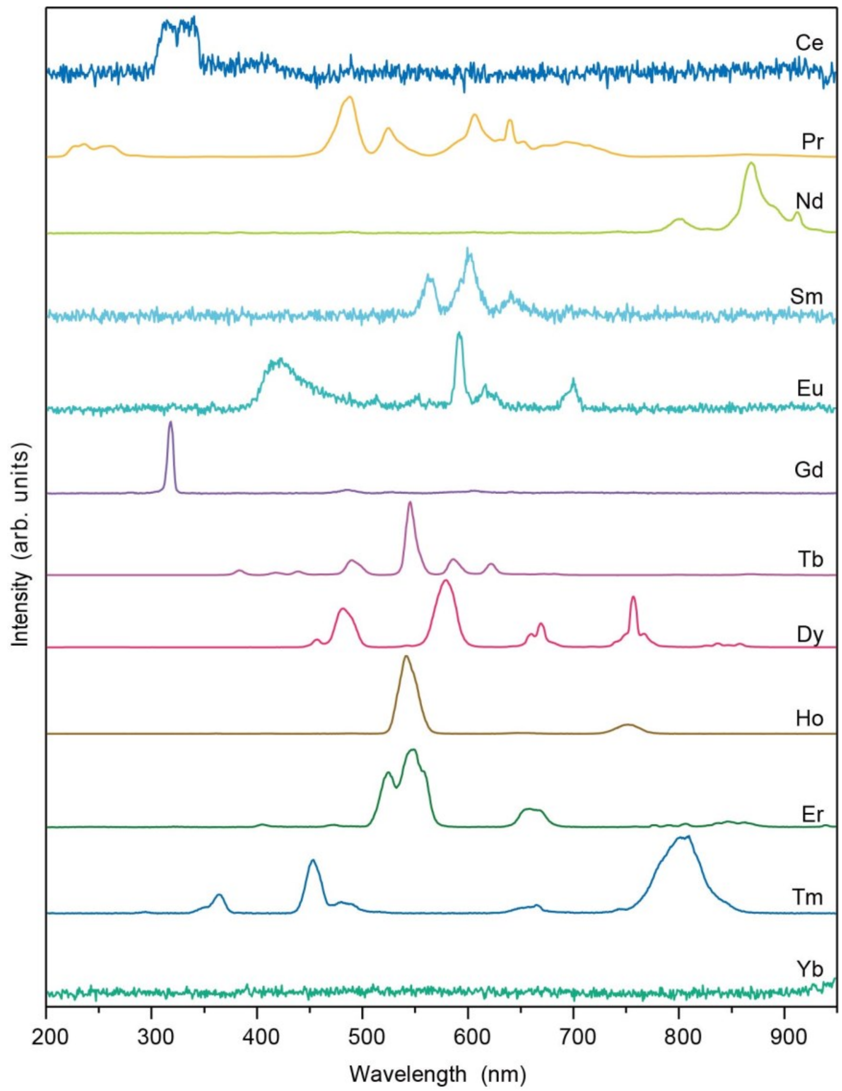

Supplementary Fig. 28 | Mechanoluminescence spectra of SrF_2 doped with different lanthanides (0.5%mol) after X-ray irradiation over the 200–950 nm range.

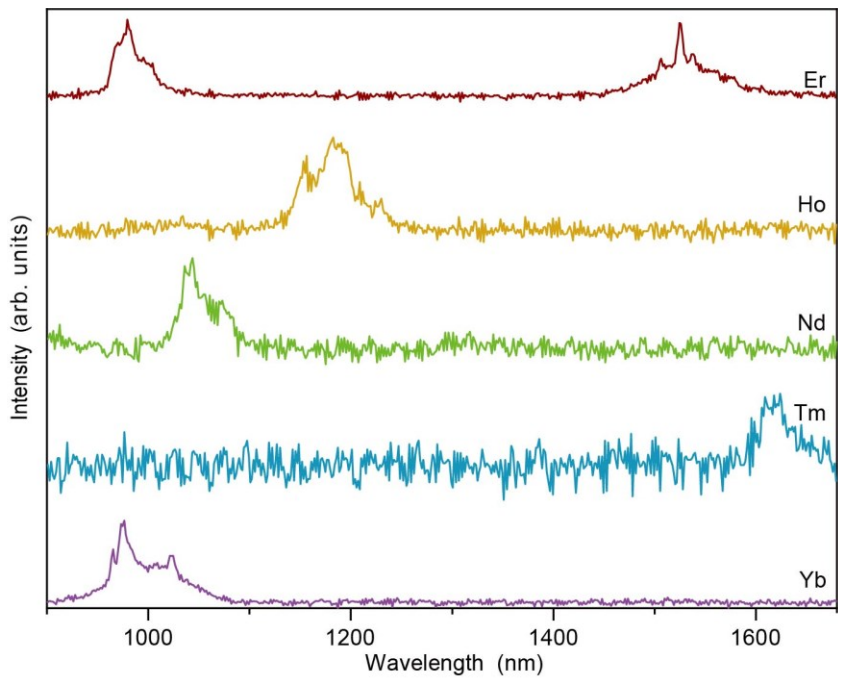

Supplementary Fig. 29 | Mechanoluminescence spectra of SrF_2 doped with different lanthanides (0.5%mol) after X-ray irradiation over the 900–1680 nm range.

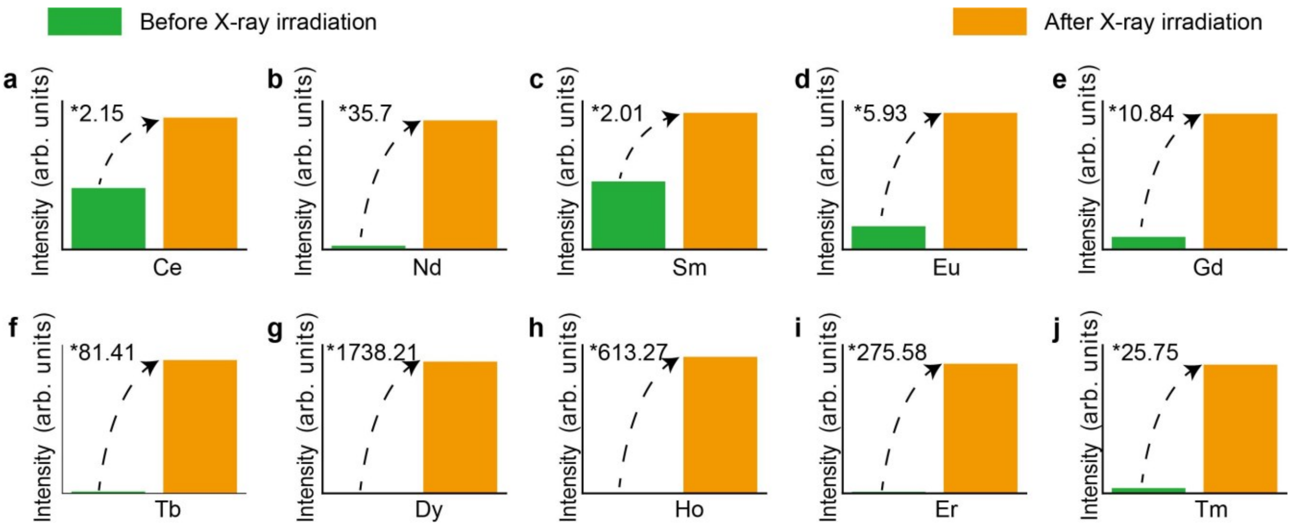

Supplementary Fig. 30 | Comparison of mechanoluminescence intensity of SrF_2 doped with different lanthanides (0.5%mol) before and after X-ray irradiation. **a** Ce, **b** Nd, **c** Sm, **d** Eu, **e** Gd, **f** Tb, **g** Dy, **h** Ho, **i** Er and **j** Tm.

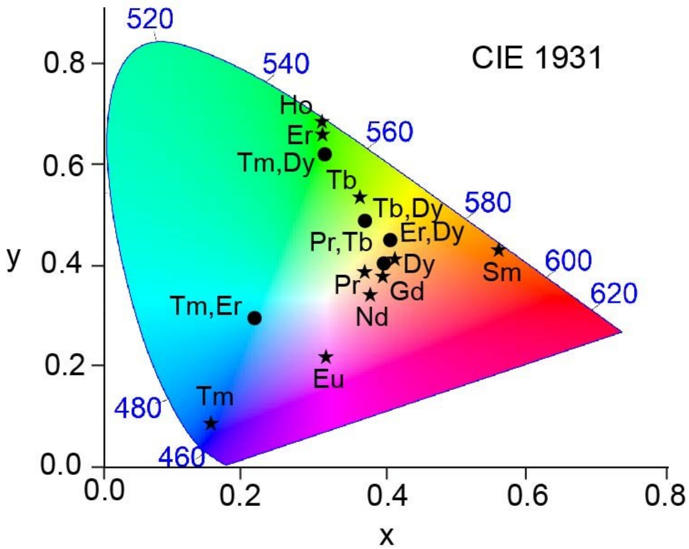

Supplementary Fig. 31 | Commission Internationale de l'Éclairage (CIE) chromatic coordinates of mechanoluminescence from SrF_2 doped with different lanthanides (0.5%mol). Circle symbols represent doubly doped samples with both dopants in 0.5%mol concentration.

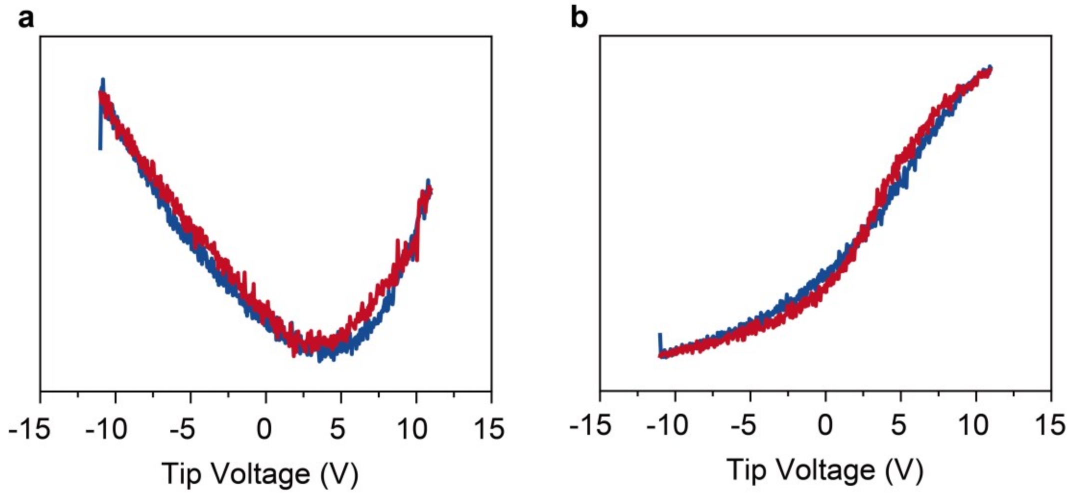

Supplementary Fig. 32 | Amplitude curves (bi-directional bias) and ferroelectric phase curve of SrF_2. **a** Amplitude curve. The red and blue curves correspond to signal variations for the bias voltage changing from -10 to +10 V and from +10 to -10 V, respectively. **b** Standard ferroelectric phase curve.

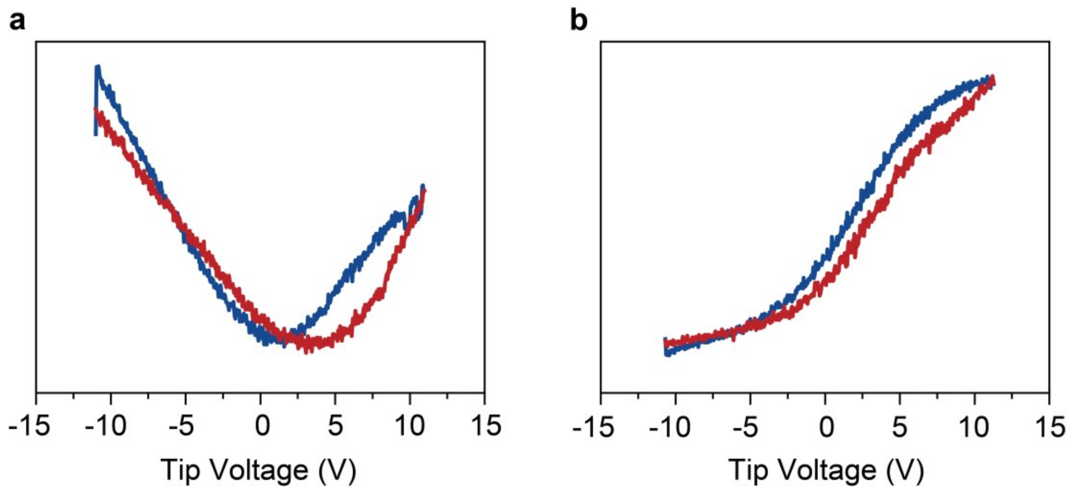

Supplementary Fig. 33 | Amplitude curves (bi-directional bias) and ferroelectric phase curve of SrF_2:0.5%Pr^{3+}. **a** Amplitude curve. The red and blue curves correspond to signal variations for the bias voltage changing from -10 to +10 V and from +10 to -10 V, respectively. **b** Standard ferroelectric phase curve.

Supplementary Table 4 | Criteria for evaluating the mechanism of mechanoluminescence (ML), summarized based on the literature.

Number	Materials	PDMS	SG/SR	PU	ER	Powder	PFM	ML mechanism	References
1	$Ca_6BaP_4O_{17}$:Ce	√	○	×	×	×	○	Triboelectrification	43
2	B_3O_3-SiO_2-ZnO:Tb/Tm/Eu	√	√	×	×	×	×	Triboelectrification	136
3	$Sr_3Al_2O_5Cl_2$:Dy	√	√	×	×	×	○	Triboelectrification	36
4	$Ca_9Bi(PO_4)_7$:Ce/Bi	√	√	×	×	×	○	Triboelectrification	44
5	$SrGa_{12}O_{19}$:Cr	√	√	×	×	×	○	Triboelectrification	83
6	CaF_2:Tb	√	√	×	×	×	×	Triboelectrification	22,23
7	$Sr_5(PO_4)_3$Cl:Eu	√	√	×	×	×	○	Triboelectrification	35
8	$Sr_3Al_2O_5Cl_2$:Eu/Tb/Ce	√	√	×	×	×	○	Triboelectrification	37
9	ZnB_2O_4:Mn	√	○	○	○	×	○	Triboelectrification	140
10	$CaZnGe_2O_6$:Mn	√	√	√	×	×	○	Triboelectrification	98
11	$BaMgAl_{12}O_{17}$:Eu	√	○	○	○	○	×	Triboelectrification	68
12	$Lu_3Al_5O_{12}$:Ce	√	√	√	×	×	√	Triboelectrification	60
13	$LiNbO_3$:Pr	○	○	○	√	○	○	Piezoelectricity	116
14	$Ca_2MgSi_2O_7$:Eu	×	○	○	√	○	○	Piezoelectricity	106
15	Ga_2O_3:Cr	√	○	○	○	○	√	Piezoelectricity	135
16	MgF_2:Yb	√	√	√	√	√	√	Piezoelectricity	19
17	$SrMg_2(PO_4)_2$:Eu	√	√	√	√	√	√	Piezoelectricity	141
18	This work	√	√	√	√	√	√	Piezoelectricity and Triboelectrification	

√ Luminous × Non-luminous ○ Lacking

PDMS: Polydimethylsiloxane; SG: Silicon gel; SR: Silicon resin; PU: Polyurethane; ER: Epoxy resin; PFM: Piezoresponse force microscopy.

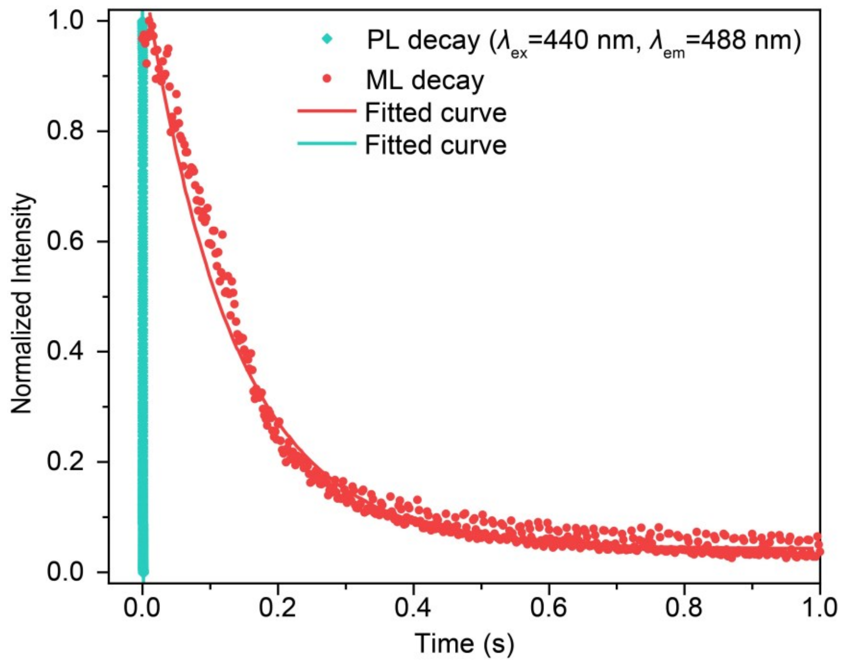

Supplementary Fig. 34 | Decay curves of photoluminescence (PL, λ_{ex}=440 nm, λ_{em}=488 nm) and trap-controlled mechanoluminescence (ML) of SrF_2:0.5%Pr^{3+}. By using the single-exponential function, the intrinsic lifetime of PL was fitted to 239 μs, a typical value of the lifetime of 4f→4f transition of Pr^{3+}. When the dynamic force was no longer applied to the sample, the trap-controlled ML continued for over 137 ms, three orders of magnitude longer than that of PL. It suggests that the processes of PL and trap-controlled ML are totally different for SrF_2:0.5%Pr^{3+}. As trap-controlled ML involves the release and migration of charge carriers, it lasts significantly longer than the PL process. Therefore, such fact could also be regarded as indirect evidence that the defects indeed participated in the trap-controlled ML.

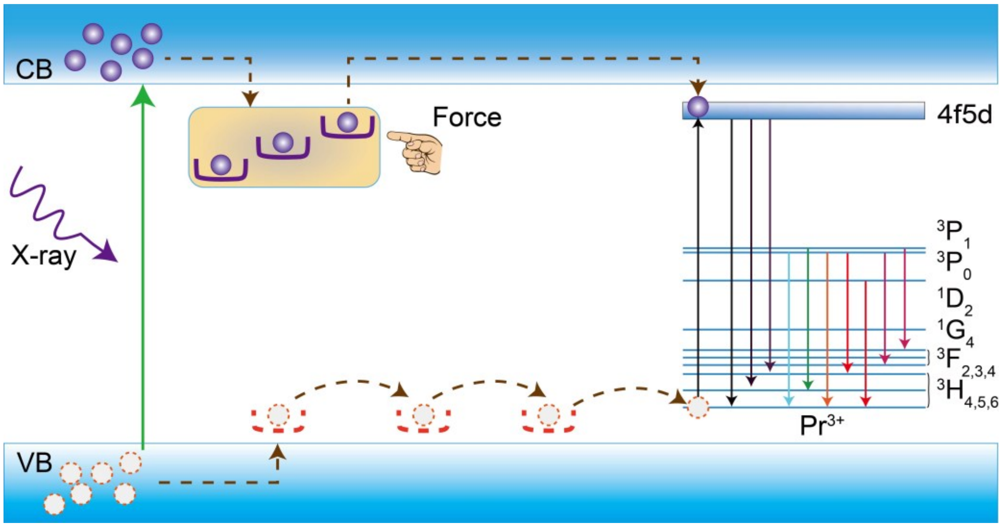

Supplementary Fig. 35 | Possible mechanism of trap-controlled mechanoluminescence behavior in Pr^{3+}-doped SrF_2. CB: conduction band; VB: valence band.

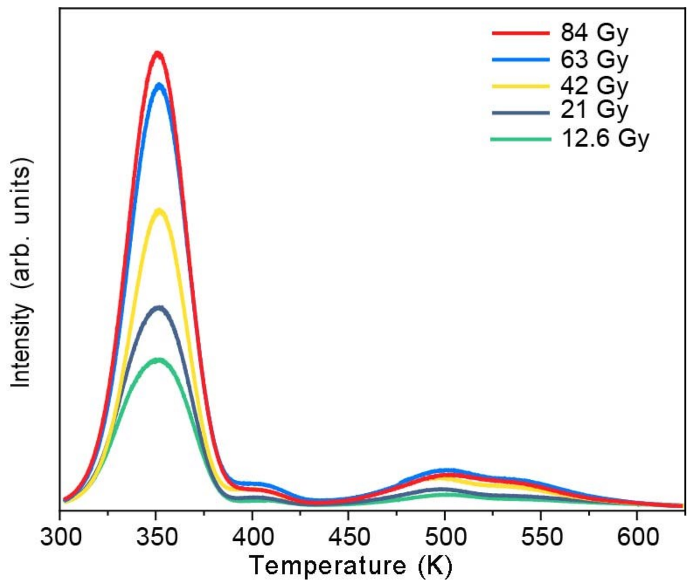

Supplementary Fig. 36 | Thermoluminescence curves of SrF_2:0.5%Pr^{3+} after being charged by X-ray of different doses (heating rate: 5 K/min).

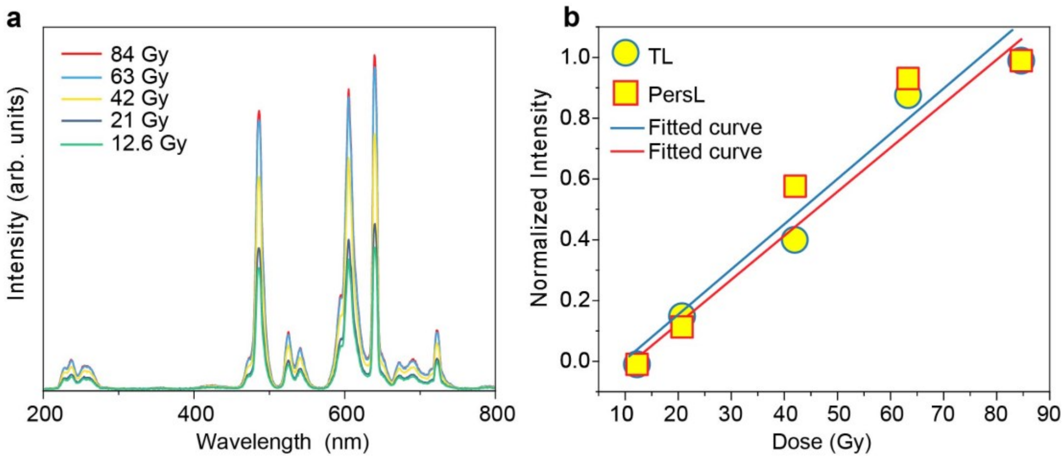

Supplementary Fig. 37 | Correlation between persistent luminescence (PersL) and thermoluminescence (TL). a PersL spectra of SrF_2:0.5%Pr^{3+} after being charged by X-ray of different doses, collected at 2 min after the stoppage of X-ray. **b** Comparison of normalized PersL intensity of the spectra shown in **a** and normalized TL intensity of the curves shown in Supplementary Fig. 36.

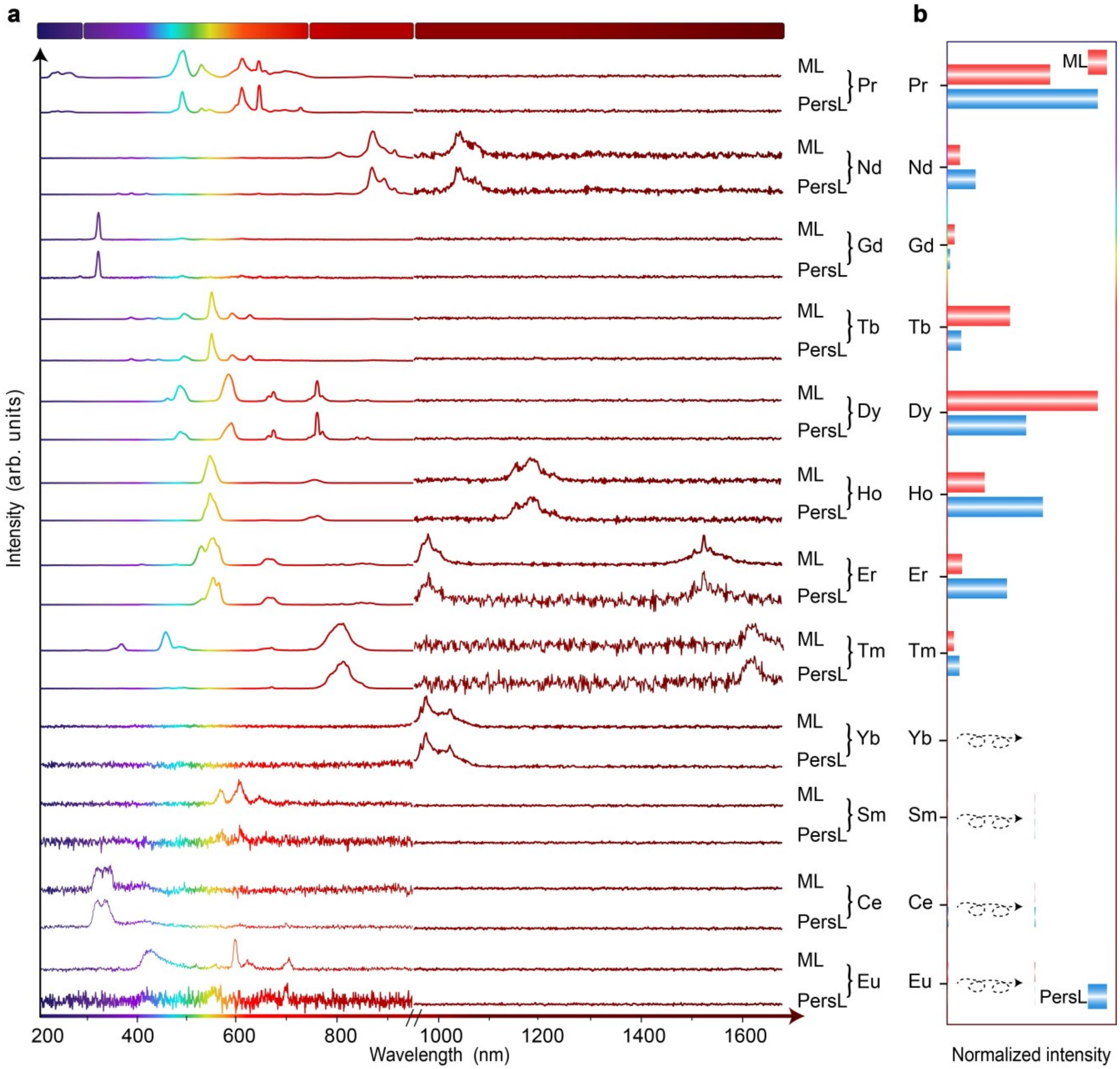

Supplementary Fig. 38 | Correlation between mechanoluminescence (ML) and persistent luminescence (PersL). a Comparison of ML and PersL spectra of SrF_2 doped with different lanthanides (0.5%mol) after 5 min of X-ray irradiation. **b** Comparison of ML and PersL intensities of SrF_2 doped with different lanthanides (0.5%mol).

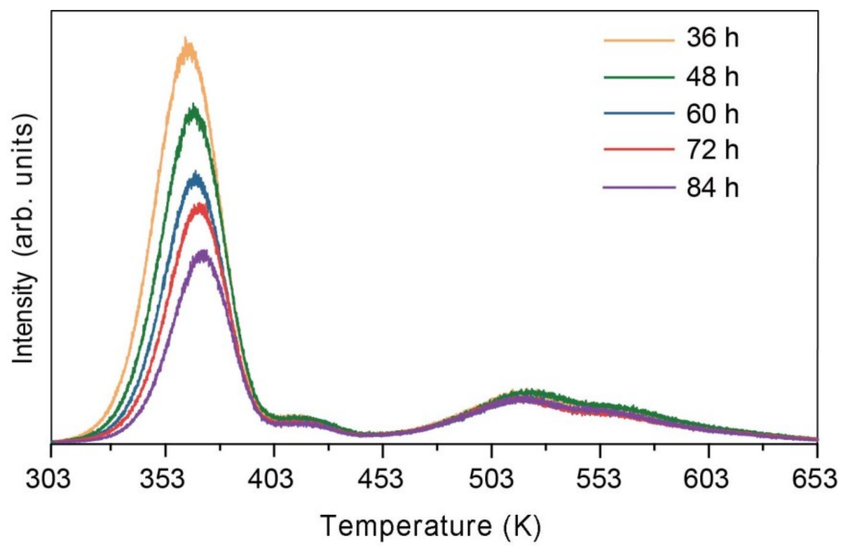

Supplementary Fig. 39 | Thermoluminescence curves of SrF_2:0.5%Pr^{3+} with various waiting times post-charging after 5 min of X-ray irradiation (heating rate: 5 K/min).

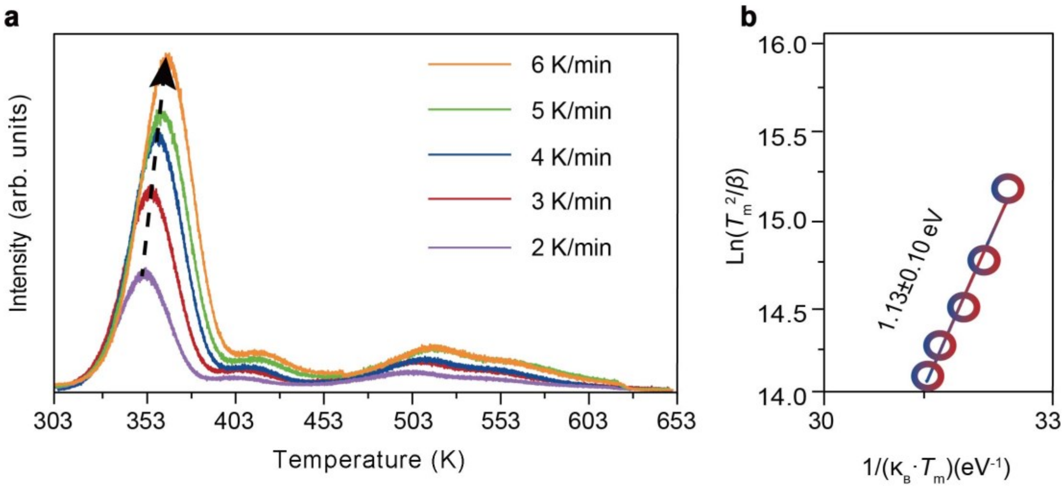

Supplementary Fig. 40 | Analysis of trap distribution. a Thermoluminescence curves of SrF_2:0.5%Pr^{3+} measured after 5 min of X-ray irradiation with different heating rates. **b** Fitted trap depth derived from **a**. By using the heating rate method, we estimated the depth of the main trap to be 1.13 eV. T_m: The temperature (in K) at the maximum of the thermoluminescence glow peak. β: Heating rate (in K/s). k: Boltzmann constant.

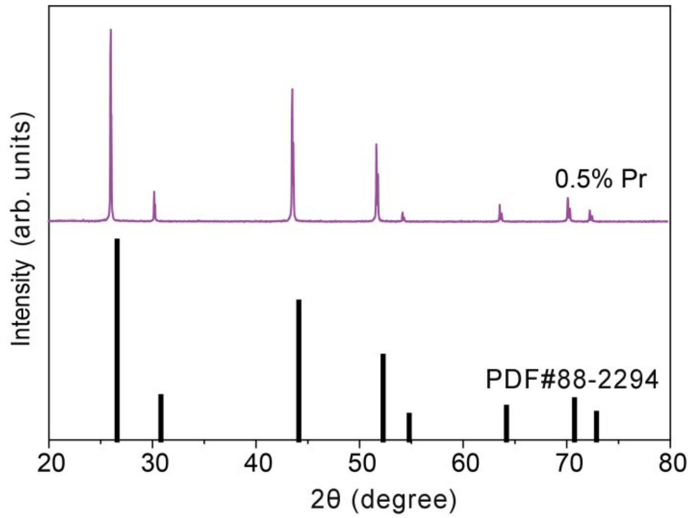

Supplementary Fig. 41 | X-ray diffraction patterns of SrF_2:0.5%Pr^{3+} after 10 min of X-ray irradiation.

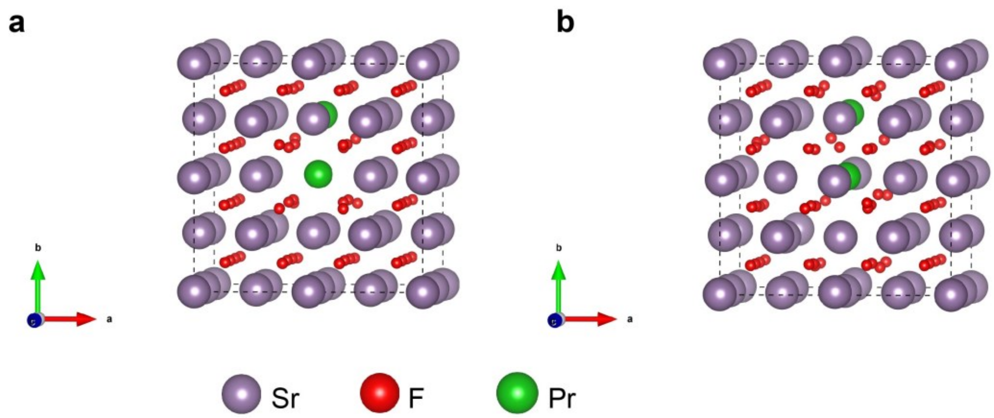

Supplementary Fig. 42 | Charge compensation mechanisms. Two specific kinds of defects in SrF_2 crystal, including Tb^{3+} replacing Sr^{2+} $[Tb_{Sr}]^{+}$, Sr vacancy $[V_{Sr}]^{2-}$ and F vacancy $[V_F]^{+}$, taking 6.25% Pr^{3+} doping as an example. **a** Two Tb^{3+} ions substituting for two Sr^{2+} ions, with charge neutrality maintained by the creation of one Sr vacancy, described as $2[Tb_{Sr}]^{+}+[V_{Sr}]^{2-}$. **b** Two Tb^{3+} ions substituting for two Sr^{2+} ions, with charge neutrality maintained by the simultaneous formation of two F vacancies and two Sr vacancies, expressed as $2[Tb_{Sr}]^{+}+2[V_F]^{+}+2[V_{Sr}]^{2-}$. The atomic coordinates of the optimized computational models are provided in the Source Data file as data.

Supplementary Table 5 | Density functional theory calculated cohesive energies (E_{coh}) for the different defects in the SrF_2 crystal, including $2[Pr_{Sr}]^{+}+[V_{Sr}]^{2-}$ and $2[Tb_{Sr}]^{+}+2[V_F]^{+}+2[V_{Sr}]^{2-}$.

Defects	Number of atoms (N)	Supercell E_s (eV)	Free state energy (eV)			Cohesive energies E_{coh} (eV)
			E_{Sr}	E_F	E_{Pr}	
$2[Pr_{Sr}]^{+}+[V_{Sr}]^{2-}$	95	-546.93	-0.02	-0.45	-0.19	-5.44
$2[Tb_{Sr}]^{+}+2[V_F]^{+}+2[V_{Sr}]^{2-}$	92	-526.90	-0.02	-0.45	-0.19	-5.41

Supplementary Note 1 | Charge compensation mechanisms.

Supplementary Table 5 presents the calculated cohesive energies of the cell (E_{coh}) corresponding to different defects within the SrF_2 crystal. The definition of E_{coh} is as follows: $E_{coh} = (E_s - a \times E_{Sr} - b \times E_F - c \times E_{Pr})/N$, where E_s represents the total energy of the supercell, E_{Sr}, E_F and E_{Pr} are the free state energies of the Sr, F and Pr atoms, respectively; a, b and c denote the numbers of the corresponding atomic species in the supercell; and N is the total number of atoms in the supercell. The results indicate that the atomic E_{coh} (-5.44 eV) for the $2[Pr_{Sr}]^{+}+[V_{Sr}]^{2-}$ defect cluster is the smallest. It means that two Pr^{3+} dopants would replace two Sr^{2+} cations in the SrF_2 crystal, resulting in one Sr^{2+} vacancy to keep the charge balance.

Supplementary Fig. 43 | A quick response (QR) code made of SrF_2:0.5%Pr^{3+} for inspection at customs. Upon exposure to X-ray irradiation, the QR code is charged. After the release of room temperature persistent luminescence, force stimulation can be applied to the QR code to achieve mechanoluminescence for secondary inspection.

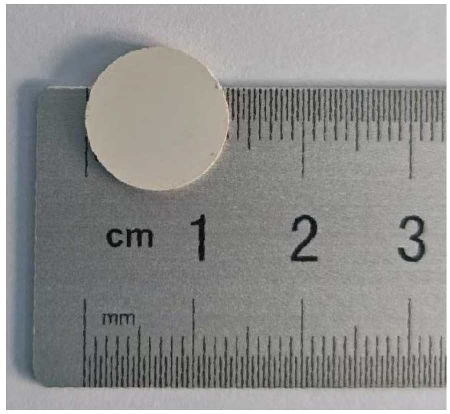

Supplementary Fig. 44 | Photograph of the SrF_2:0.5%Pr^{3+} disk with a diameter of 13 mm.

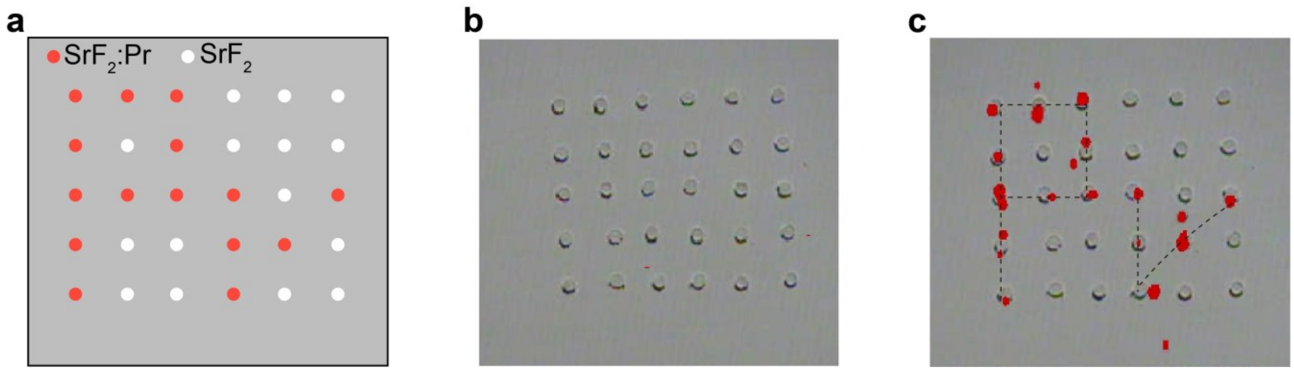

Supplementary Fig. 45 | Information storage and reading depending on UVC luminescence. a Schematic diagram of 5*6 array. The white and red dots represent SrF_2 and SrF_2:Pr^{3+}, respectively. **b** Photograph of the array before X-ray irradiation. **c** Photograph of the array after being charged by X-ray for 5 min. The hidden patterns ‘P’ and ‘r’ can be captured by a solar blind camera (dotted line).

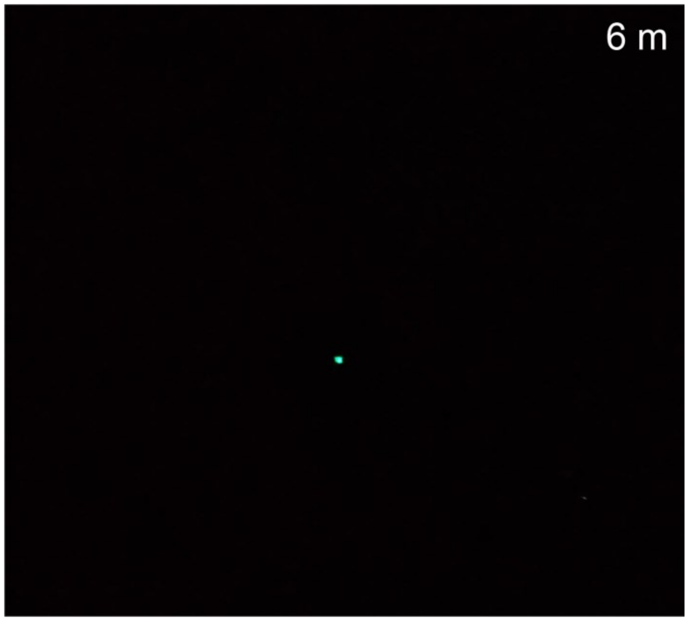

Supplementary Fig. 46 | Photograph of ZnS:Cu^{2+}@polydimethylsiloxane in dark environment upon stretching, taken from a distance of 6 m.

Supplementary Fig. 47 | Demonstration of outdoor emergency rescue by using UVC photon. A person is trapped in an outdoor hazardous situation where visibility is limited. In this case, it is difficult to identify the trapped person. At this moment, the stretchable elastic film made of $SrF_2:Pr^{3+}$@polydimethylsiloxane might work. The trapped person pulls the $SrF_2:Pr^{3+}$@polydimethylsiloxane film and the UVC mechanoluminescence can be located using a solar blind camera by rescue personnel. Such strategy, together with other rescue technologies, is expected to effectively enhance the efficiency of rescue operations.

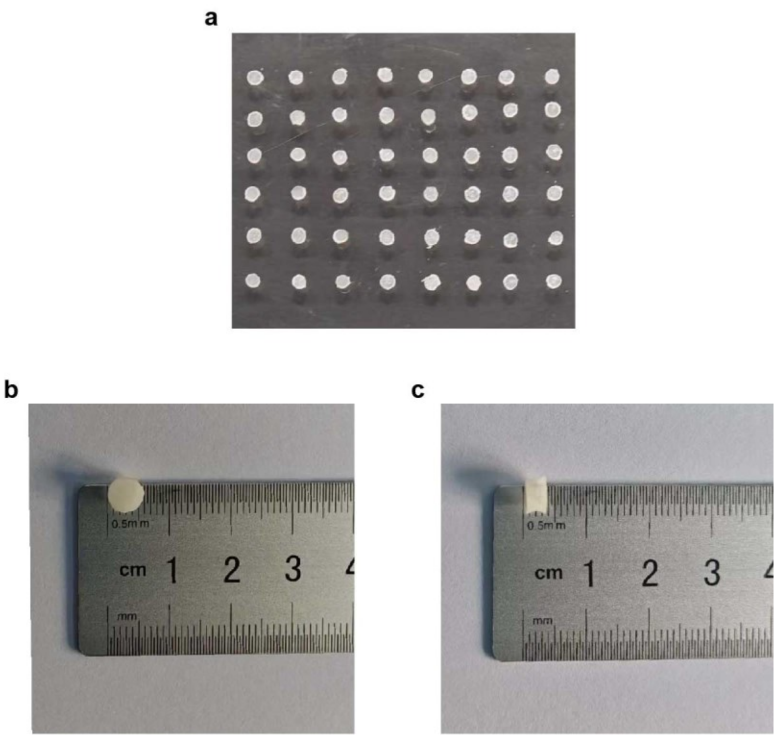

Supplementary Fig. 48 | SrF_2:$Ln^{2+,3+}$@polydimethylsiloxane array. a Photograph of SrF_2:$Ln^{2+,3+}$@polydimethylsiloxane arranged in an 8*6 array. **b** Diameter demonstration, and **c** Thickness demonstration of a single SrF_2:$Ln^{2+,3+}$@polydimethylsiloxane cylinder.

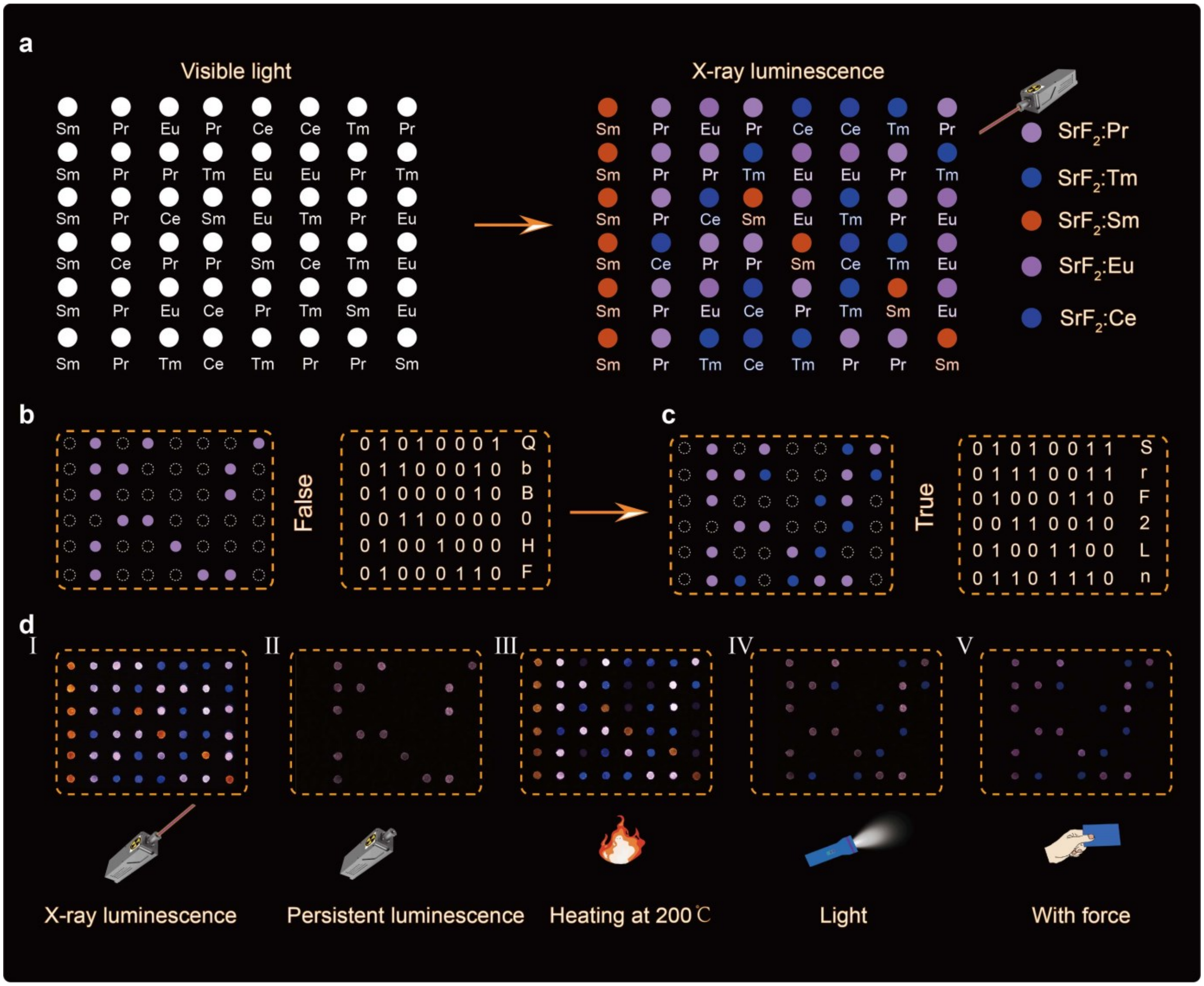

Supplementary Fig. 49 | Information storage and encryption based on SrF_2:$Ln^{2+,3+}$. a Schematic of the mechanoluminescent array using SrF_2:$Ln^{2+,3+}$@polydimethylsiloxane. **b** Luminescence array with false information. **c** Luminescence array with correct information. **d** Multimodal luminescence array: (I) X-ray on; (II) X-ray off; (III) Heat treatment; (IV) Optical stimulation; (V) Force stimulation.

Supplementary Note 2 | Applications based on visible light.

We introduced a novel binary encoding method by using $SrF_2:Ln^{2+,3+}$. By incorporating $SrF_2:Ln^{2+,3+}$ (Ln = Pr^{3+}, Tm^{3+}, Sm^{3+}, $Eu^{2+,3+}$ and Ce^{3+}) into polydimethylsiloxane (PDMS), we designed an 8*6 cylindrical array (Supplementary Figs. 48 and 49a). Under daylight, these cylinders all appeared the same. After exposure to X-ray, the cylindrical array became colorful due to the characteristic emissions of dopant luminescent centers. The correct information was hidden by different combinations of luminescence (Supplementary Figs. 49b and 49c). When the array was subjected to X-ray irradiation or heated after exposure to X-ray irradiation, all samples emitted light without conveying any useful message (Supplementary Figs. 49d-I and 49d-III). After switching off the X-ray source for 5 min, the persistent luminescence (PersL) of $SrF_2:Pr^{3+}$ was far stronger than that of others, resulting in the false information 'QbB0HF' (Supplementary Fig. 49d-II). Under the stimulation of photon or force, the luminescence of $SrF_2:Pr^{3+}$ and $SrF_2:Tm^{3+}$ provided the correct information 'SrF2Ln' (Supplementary Figs. 49d-IV and 49d-V). These results reveal that our binary coding based on $SrF_2:Ln^{2+,3+}$ has great potential in advanced information encryption and anti-counterfeiting technology.

Electronic signature (*e*-signature) has been widely used nowadays. However, it is easy to imitate the profile of an *e*-signature. Therefore, adding more information on *e*-signature is essential. $SrF_2:Ln^{2+,3+}$ can play a useful role in improving the security of *e*-signature. We designed a unique 'HBU' stamp and pressed it onto the $SrF_2:Pr^{3+}$@PDMS film (Supplementary Fig. 50), leaving there a 'HBU' pattern with different luminescence distribution. We fetched the mechanoluminescence (ML) information from the points of a, b and c and then calculated the intensity ratio of a/b, a/c and b/c. By defining a unit as a threshold, the obtained intensity ratios were found to be [100]. In this way, we added information to *e*-signature.

We also expanded the application potential of $SrF_2:Pr^{3+}$ for non-destructive examination. In the beginning, $SrF_2:Pr^{3+}$ was coated on the surface of automotive tires. During non-destructive inspection by X-ray, the coated $SrF_2:Pr^{3+}$ was pre-charged. Thereafter, by means of PersL or ML from the $SrF_2:Pr^{3+}$, the worker and consumer can confirm whether or not the tire had passed the inspection before leaving the factory and after buying the tire, respectively (Supplementary Fig. 51). To ensure high quality, tires usually undergo friction test in factory. Since friction generates heat, the PersL intensity ratio of $^3P_1 \rightarrow ^3H_5$ to $^3P_0 \rightarrow ^3F_2$ transitions of $SrF_2:Pr^{3+}$ can also be used to monitor the temperature during friction testing.

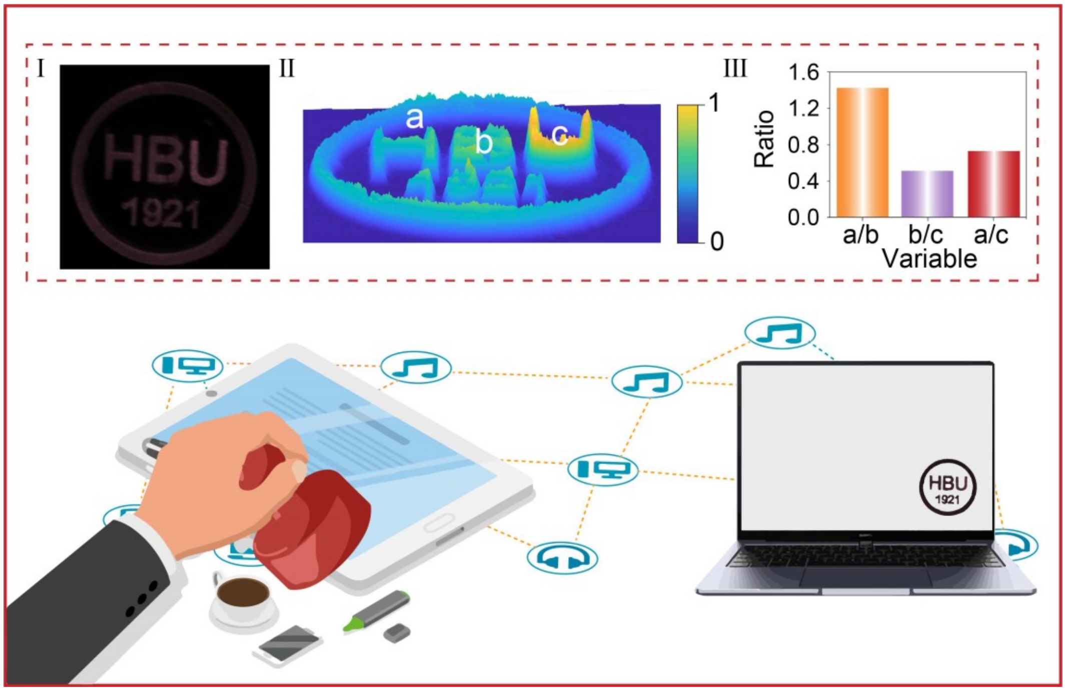

Supplementary Fig. 50 | Electronic seal. (I) Visualization of 'HBU' stamp through UVC mechanoluminescence (ML). (II) Distribution of ML intensity of 'HBU' stamp extracted from (I). (III) ML intensity ratios between different points at a, b and c.

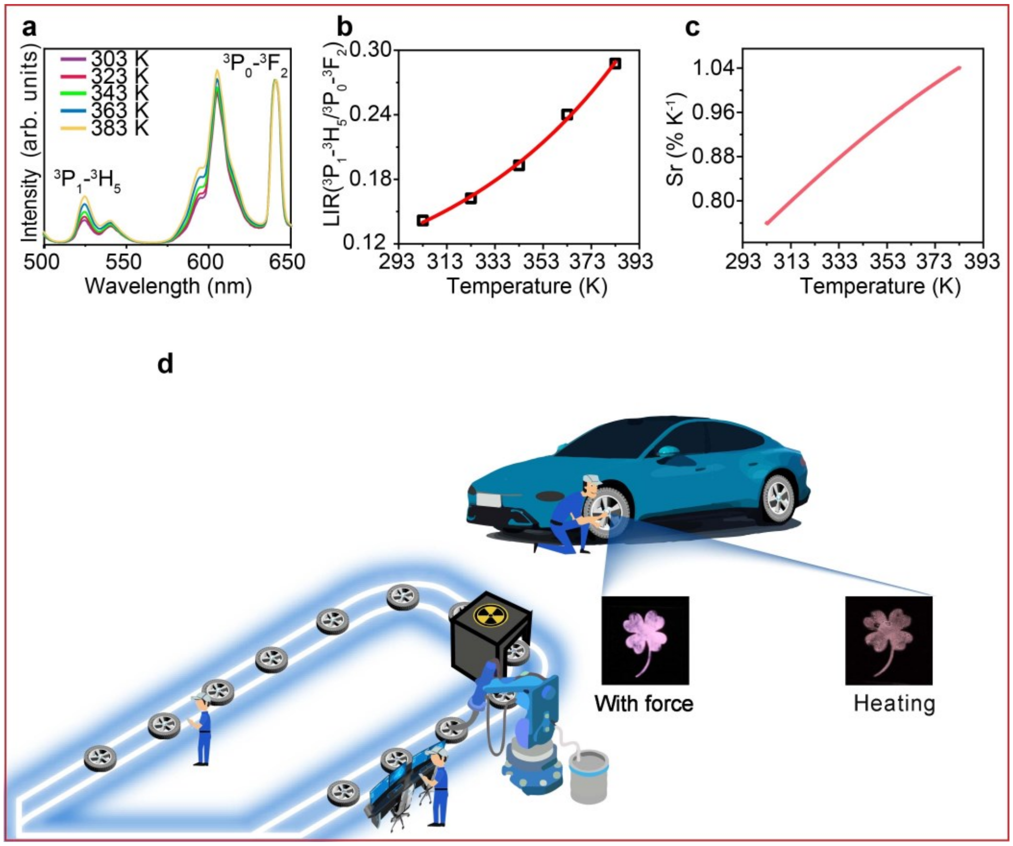

Supplementary Fig. 51 | Nondestructive testing application. a Emission spectra of SrF_2:0.5%Pr^{3+} upon different thermal stimulations after 5 min of X-ray irradiation. **b** Luminescence intensity ratio (LIR) between the $^3P_1 \rightarrow ^3H_5$ and $^3P_0 \rightarrow ^3F_2$ transition of Pr^{3+}, and **c** Relative sensitivity (S_r) of designed ratiometric thermometry as a function of temperature. **d** Schematic diagram of non-destructive testing by using SrF_2:0.5%Pr^{3+}.

Supplementary references

1. Du, Y. et al. Mechanically excited multicolor luminescence in lanthanide ions. *Adv. Mater.* **31**, 1807062 (2019).

2. Li, L., Wondraczek, L., Peng, M., Ma, Z. & Zou, B. Force-induced 1540 nm luminescence:role of piezotronic effect in energy transfer process for mechanoluminescence. *Nano Energy.* **69**, 104413 (2020).

3. Li, X. et al. Broadband multimodal emission in Sb-doped CaZnOS-layered semiconductors. *Sci China Mater* **65**, 1329–1336 (2022).

4. Tu, D. et al. Mechanism of mechanical quenching and mechanoluminescence in phosphorescent CaZnOS:Cu. *Light:Sci. Appl.* **4**, e356–e356 (2015).

5. Yang, Y. L. et al. Time-resolved bright red to cyan color tunable mechanoluminescence from CaZnOS:Bi^{3+},Mn^{2+} for anti-counterfeiting device and stress sensor. *Adv. Opt. Mater.* **9**, 2100668 (2021).

6. Zhang, J. C. et al. An intense elastico-mechanoluminescence material CaZnOS:Mn^{2+} for sensing and imaging multiple mechanical stresses. *Opt. Express.* **21**, 12976–12986 (2013).

7. Chen, C. et al. Creating visible-to-near-infrared mechanoluminescence in mixed-anion compounds $SrZn_2S_2O$ and SrZnSO. *Nano Energy.* **68**, 104329 (2020).

8. Lin, F. et al. Modeling polyhedron distortion for mechanoluminescence in mixed-anion compounds RE_2O_2S:Ln^{3+}. *Chem. Mater.* **34**, 5311–5319 (2022).

9. Han, Y. et al. Application convenient and energy-saving mechano-optics of Er^{3+}-doped X_2O_2S (X=Y/Lu/Gd) for thermometry. *J. Mater. Chem. C.* **11**, 16143–16151 (2023).

10. Kaur, J., Dubey, V. & Suryanarayana, N. Comparative study of ML and PL spectra of different impurity-doped (Zn,Cd)S mixed phosphors. *Res. Chem. Intermed.* **39**, 4337–4349 (2013).

11. Jia, J., Gao, X. & Zou, G. Alkaline-earth-metal-ions blending enhanced self-activated and Bi^{3+}-activated mechanoluminescence from $Ca_{1-x}Ba_xZnOS$. *Adv. Funct. Mater.* **32**, 2207881 (2022).

12. Li, L., Wong, K. L., Li, P. & Peng, M. Mechanoluminescence properties of Mn^{2+}-doped BaZnOS phosphor. *J. Mater. Chem. C.* **4**, 8166–8170 (2016).

13. Rao, N. M., Reddy, D. R., Reddy, B. & Xu, C. Intense red mechanoluminescence from $(ZnS)_{1-x}$(MnTe). *Phys. Lett. A.* **372**, 4122–4126 (2008).

14. Zhou, T. et al. Unrevealing temporal mechanoluminescence behaviors at high frequency via piezoelectric actuation. *Small.* **19**, 2207089 (2023).

15. Xu, C., Watanabe, T., Akiyama, M. & Zheng, X. Artificial skin to sense mechanical stress by visible light emission. *Appl. Phys. Lett.* **74**, 1236–1238 (1999).

16. Chandra, V., Chandra, B. & Jha, P. Self-recovery of mechanoluminescence in ZnS:Cu and ZnS:Mn phosphors by trapping of drifting charge carriers. *Appl. Phys. Lett.* **103**, 16 (2013).

17. Cai, C. et al. All-lanthanide mechanoluminescence from transparent Ln-doped MgF_2@ elastomer for Flexible and Stretchable Lighting and Stress Sensing. *Adv. Mater. Technol.* **9**, 2301855 (2024).

18. Li, P. et al. Mechanically induced photons from ultraviolet-c to near-infrared in Tm^{3+}-doped MgF_2. *Opt. Express.* **31**, 22396–22404 (2023).

19. Guo, L. et al. Visual representation of the stress distribution with a color-manipulated mechanoluminescence of fluoride for structural mechanics. *Adv. Funct. Mater.* **33**, 2306875 (2023).

20. Ning, J. et al. MgF_2:Mn^{2+}: novel material with mechanically-induced luminescence. *Sci. Bull.* **67**, 707–715 (2022).

21. Li, L. et al. Ultraviolet light charged and self-powered mechanoluminescence of $KMgF_3$:Tb^{3+} glass ceramics in various media. *Ceram. Int.* **50**, 56043–56049 (2024).

22. Wang, W., Wang, S., Gu, Y., Zhou, J. & Zhang, J. Contact-separation-induced self-recoverable mechanoluminescence of CaF_2:Tb^{3+}/PDMS elastomer. *Nat. Commun.* **15**, 2014 (2024).

23. Wang, M. et al. Visualization of strain rate based on mechanoluminescence tailing. *Chem. Eng. J.* **502**, 157876 (2024).

24. Wang, C. et al. Enabling multimodal luminescence in a single nanoparticle for X-ray imaging encryption and anticounterfeiting. Nano Lett. **24**, 9691-9699 (2024).

25. Li, L. et al. Ultraviolet-c mechanoluminescence from $NaYF_4$:Pr^{3+}. *Appl. Phys. Lett.* **124**, 10 (2024).

26. Li, L. et al. Persistent-and mechanoluminescence of Er^{3+}-Doped $NaYF_4$ for multipurpose use. *Small. Methods*, 2401615. (2025).

27. Peng, S. et al. Mechano-luminescence behavior of lanthanide-doped fluoride nanocrystals for three-

dimensional stress imaging. *ACS nano.* **17**, 9543-9551 (2023).

28. Lu, L. et al. Visualized X-ray dosimetry for multienvironment applications. *Nano Lett.* **23**, 8753–8760 (2023).

29. Li, L. et al. Stress-triggered mechanoluminescence in ZnO-based heterojunction for flexible and stretchable mechano-optics. *Adv. Funct. Mater.* **33**, 2301372 (2023).

30. Zhang, J.C. et al. Ultra-long-delay sustainable and short-term-friction stable mechanoluminescence in Mn^{2+}-activated $NaCa_2GeO_4F$ with centrosymmetric structure. *Chem. Eng. J.* **406**, 126798 (2021).

31. Du, R. et al. Triboelectrification-induced mechanoluminescence of isomorphic Sr_3MO_4F:Ln (M=Al,Ga):Performance and difference. *Chem. Eng. J.* **499**, 156273 (2024).

32. Han, L. et al. Lead-free perovskite with efficient tellurium ion activation for multifunctional applications. *Small.* **20**, 2403295 (2024).

33. Yin, B. et al. Mechanoluminescence from $CaCl_2$:Eu^{2+}. *J. Lumin.* **275**, 120781 (2024).

34. Chandra, B., Elyas, M. & Majumdar, B. Dislocation models of mechanoluminescence in γ-and X-irradiated alkali halides crystals. *Solid State Commun.* **42**, 753–757 (1982).

35. Ma, Z., Fang, S., Bai, Y., Wei, W. & Wang, Z. Efficient blue mechanoluminescence in Eu^{2+}-activated $Sr_5(PO_4)_3Cl$ for advanced anticounterfeiting with mildew-resistant behavior. *Mater. Today Chem.* **36**, 101917 (2024).

36. Bai, Y. et al. Self-charging persistent mechanoluminescence with mechanics storage and visualization activities. *Adv. Sci.* **9**, 2203249 (2022).

37. Bai, Y. et al. Interfacial triboelectrification-modulated self-recoverable and thermally stable mechanoluminescence in mixed-anion compounds. *Nano Energy.* **96**, 107075 (2022).

38. Meng, W., Cai, P., Fu, X. & Zhang, H. Sensitive mechanoluminescence from Eu^{2+}, Tm^{3+} co-doped $Sr_3Al_2O_5Cl_2$ phosphors. *J. Lumin.* **248**, 118983 (2022).

39. Du, R. K. et al. Synergistic mechanoluminescence and mechanochromism via triboelectrification-Iinduced Eu^{3+}/Eu^{2+} redox shuttle. *Laser Photonics Rev.* **19**, 2401211 (2025).

40. Ou, J. et al. Awakening dumb Mn^{2+} mechanoluminescence site to achieve force, temperature and time-

domain induced color tuning via trap-assisted energy transfer. *Chem. Eng. J.* **493**, 152500 (2024).

41. Suo, H. et al. Excitation-mode-selective emission through multiexcitonic states in a double perovskite single crystal. *Light:Sci. Appl.* **14**, 21 (2025).

42. Yan, S. et al. Mechanoluminescence from lead-free perovskites Cs_2HfCl_6:Te^{4+}. *Laser Photonics Rev.* 2401236. (2025)

43. Qin, S. et al. Self-recoverable, highly repeatable, and thermally stable mechanoluminescence for dual-mode information storage and photonic skin applications. *Adv. Funct. Mater.* **34**, 2401535 (2024).

44. Ma, Z., Han, Y., Bai, Y., Liu, B. & Wang, Z. Near-ultraviolet and deep red dual-band mechanoluminescence for color manipulation and biomechanics detection. *Chem. Eng. J.* **456**, 141122 (2023).

45. Kamimura, S., Yamada, H. & Xu, C.N. Development of new elasticoluminescent material $SrMg_2(PO_4)_2$:Eu. *J. Lumin.* **132**, 526–530 (2012).

46.Van den Eeckhout K, Smet PF, & Poelman D. Persistent luminescence in Eu^{2+}-doped compounds:a review. *Materials* **3**, 2536–2566 (2010).

47. Ju, G., Hu, Y., Chen, L., Wang, X. & Hung, L. Persistent luminescence properties of $SrMg_2(PO_4)_2$:Eu^{2+},Tb^{3+}. *Appl. Phys. A:Mater. Sci. Process.* **114**, 867–874 (2014).

48. Zhang, J. C. Xu, C. N. & Long, Y. Z. Elastico-mechanoluminescence in $CaZr(PO_4)_2$:Eu^{2+} with multiple trap levels. *Opt. Express.* **21**, 13699–13709 (2013).

49. Fukuda, K. & Fukutani, K. Crystal structure of calcium zirconium diorthophosphate, $CaZr(PO_4)_2$. *Powder Diffr.* **18**, 296–300 (2003).

50. Zhang, J. C. et al. Eu^{2+}/Eu^{3+}-emission-ratio-tunable $CaZr(PO_4)_2$: Eu phosphors synthesized in air atmosphere for potential white light-emitting deep UV LEDs. *J. Mater. Chem. C.* **2**, 312–318 (2014).

51. Zhang, P. et al. Multicolor mechanoluminescence for integrated dual-mode stress and temperature sensing. *Inorg. Chem. Front.* **12**, 2315–2324 (2025).

52. Zhou, S., Cheng, Y. & Wang, Y. Thermally recovered mechanoluminescence in $Ca_6BaP_4O_{17}$:Eu^{2+}. *Opt. Lett.* **49**, 1908–1910 (2024).

53. Wang, T. et al. Trap assisted dynamic mechanoluminescence toward self-referencing and visualized strain sensing. *Adv. Sci.* **12**, 2410673 (2025).

54. Zhou, S., Cheng, Y., Xu, J., Lin, H. & Wang, Y. Ratiometric mechanoluminescence of double-activator doped phosphatic phosphors: color-resolved visualization of stress-sensing and quantified evaluation for sensing performance. *Adv. Funct. Mater.* **32**, 2208919 (2022).

55. Li, H., Yang, Y., Li, P., Peng, D. & Li, L. Force-induced ultraviolet C luminescence of Pr^{3+}-doped $Sr_2P_2O_7$ for X-Ray dosimetry. *Adv. Mater.* **36**, 2411804 (2024).

56. Cheng, K. et al. A universal strategy for multicolor mechanoluminescence via radiative energy transfer based on ultraviolet mechanoluminescent material $Ca_9Al(PO_4)_7:Ce^{3+}$. *Laser Photonics Rev.* 2401524 (2025).

57. Feng, L. et al. Mechanically charged and self-recoverable green-emitting long-persistent mechanoluminescence in $Ca_9NaMg\ (PO_4)_7:Tb^{3+}$. *Inorg. Chem.* **63**, 24342–24350 (2024).

58. Huang, Z. et al. Smart mechanoluminescent phosphors:a review of strontium-aluminate-based materials, properties, and their advanced application technologies. *Adv. Sci.* **10**, 2204925 (2023).

59. Shao, P. et al. Self-recoverable NIR mechanoluminescence from Cr^{3+} doped perovskite type aluminate. *Advanced Powder Materials.* **3**, 100165 (2024).

60. Wang, W. et al. Contact electrification induced mechanoluminescence. *Nano Energy.* **94**, 106920 (2022).

61. Ma, Z. et al. Mechanics-induced triple-mode anticounterfeiting and moving tactile sensing by simultaneously utilizing instantaneous and persistent mechanoluminescence. *Mater. Horiz.* **6**, 2003–2008 (2019).

62. Liu, Z. et al. NIR mechanoluminescence from Cr^{3+} activated $Y_3Al_5O_{12}$ with intense zero phonon line. *Adv. Funct. Mater.* **33**, 2214497 (2023).

63. Zhang, H., Yamada, H., Terasaki, N. & Xu, C. N. Blue light emission from stress-activated $CaYAl_3O_7$:Eu. *J. Electrochem. Soc.* **155**, J128 (2008).

64. Zhang, H., Xu, C. N., Terasaki, N. & Yamada, H. Electro-mechano-optical luminescence from

$CaYAl_3O_7$:Ce. *Electrochem. Solid-State Lett.* **14**, J76 (2011).

65. Matsui, H. Xu, C. N. & Tateyama, H. Stress-stimulated luminescence from $ZnAl_2O_4$:Mn. *Appl. Phys. Lett.* **78**, 1068–1070 (2001).

66. Tigga, S., Brahme, N. & Bisen, D. Photoluminescence and mechanoluminescence investigation of bluish-green afterglow $SrMgAl_{10}O_{17}$:Ce^{3+} phosphor. *J. Mater. Sci.:Mater. Electron.* **28**, 4750–4757 (2017).

67. Chandra, V. & Chandra, B. Suitable materials for elastico mechanoluminescence-based stress sensors. *Opt. Mater.* **34**, 194–200 (2011).

68. Gu, Y. et al. A Bifunctional luminescent whitening and sensing material based on photoluminescence and mechanoluminescence. *Inorg. Chem.* **63**, 2577–2585 (2024).

69. Qin, S. et al. Intense and efficient green mechanoluminescence in $CaLaAl_3O_7$ through Tb^{3+} doping. *Mater. Res. Bull.* **145**, 111535 (2022).

70. Li, C. et al. Intense photoluminescence and mechanoluminescence of novel $BaLaAl_3O_7$:xEu^{3+} red nanophosphors. *Eur. J. Inorg. Chem.* **27**, e202300789 (2024).

71. Tang, Y. et al. Dynamic multicolor emissions of multimodal phosphors by Mn^{2+} trace doping in self-activated $CaGa_4O_7$. *Nat. Commun.* **15**, 3209 (2024).

72. Zhang, P. et al. High defect tolerance breaking the design limitation of full-spectrum multimodal luminescence materials. *Adv. Mater.* **37**, 2411532 (2025).

73. Hu, T. et al. A new class of battery-free, mechanically powered, piezoelectric $Ca_5Ga_6O_{14}$:Tb^{3+} phosphors with self-recoverable luminescence. *J. Mater. Chem. C* **10**, 9554–9562 (2022).

74. Yang, X. et al. Designing ratiometric mechanoluminescence via threshold manipulation in sandwich structures. *Laser Photonics Rev.* **18**, 2301004 (2024).

75. Matsui, H., Xu, C. N., Akiyama, M. & Watanabe, T. Strong mechanoluminescence from UV-irradiated spinels of $ZnGa_2O_4$:Mn and $MgGa_2O_4$:Mn. *Jpn. J. Appl. Phys.* **39**, 6582 (2000).

76. Wang, Y. et al. Simultaneous NIR photoluminescence and mechanoluminescence from Cr^{3+} activated $MgGa_2O_4$ phosphors with multifunctions for optical sensing. *J. Mater. Chem. C.* **12**, 3654–3661 (2024).

77. Chen, Z. et al. Visible-to-near-infrared mechanoluminescence in Bi-activated spinel compounds for

multiple information anticounterfeiting. *ACS Appl. Mater. Interfaces.* **16**, 35279–35292 (2024).

78. Wang, Y., Feng, P., Ding, S., Tian, S. & Wang, Y. A promising route for developing yellow long persistent luminescence and mechanoluminescence in $CaGa_2O_4:Pr^{3+}$, Li^{+}. *Inorg. Chem. Frontiers* **8**, 3748-3759 (2021).

79. Wang, J. et al. Tb^{3+}-doped $Ca_3Ga_4O_9$ phosphors with color-tunable photoluminescence and non-pre-irradiation mechanoluminescence for multimodal applications. *Adv. Opt. Mater.* **12**, 2401115 (2024).

80. Hu, T. et al. A self-recoverable mechano-photonic phosphor for high-level anti-counterfeiting. *Mater. Today Chem.* **44**, 102553 (2025).

81. Liu, S. et al. Near-infrared mechanoluminescence of Cr^{3+} doped gallate spinel and magnetoplumbite smart materials. *Adv. Funct. Mater.* **33**, 2209275 (2023).

82. Wang, Y. et al. Multi-mode luminescence in smart near-infrared Cr^{3+}/Pr^{3+} codoped $SrGa_{12}O_{19}$ phosphors induced by three distinct excitation mechanisms. *ACS Appl. Mater. Interfaces.* **16**, 33855–33864 (2024).

83. Yu, S. et al. Self-recoverable and cyclically stable near-infrared mechanoluminescence for dual-mode mechanics visualization and biomechanics detection. *Chem. Eng. J.* **474**, 145542 (2023).

84. Yang, X. et al. Energy focusing reinforced narrowband ultraviolet-B mechanoluminescence for bright-field stress visualization. *J. Mater. Chem. C.* **11**, 6912–6919 (2023).

85. Li, M. et al. Piezoelectric-induced mechanoluminescence in centrosymmetric $Lu_3Al_5O_{12}$ properties of self-recoverable and tunable near-infrared luminescence. *Chem. Eng. J.* **500**, 156715 (2024).

86. Wu, S. et al. Single Tb^{3+} ion doped ratiometric mechanoluminescence for tunable stress visualization. *Chem. Eng. J.* **469**, 143961 (2023).

87. Duan, J. et al. Environmentally tolerable and self-recoverable mechanoluminescent materials with long wave for flexible mechanical visualization. *J. Alloys Compd.* **1010**, 177383 (2025).

88. Shi, R. et al. Luminescence properties of a green-emitting mechanoluminescent phosphor $CaSrGa_4O_8:xTb^{3+}$ without pre-excitation. *RSC Adv.* **14**, 10726–10735 (2024).

89. Sun, Q. et al. Intense and sensitive green mechanoluminescence by Tb^{3+} doping in Y_3GaO_6. *Ceram.*

Int. **50**, 44417–44425 (2024).

90. Zhang, N. et al. Intense mechanoluminescence in undoped $LiGa_5O_8$ with persistent and recoverable behaviors. *Adv. Opt. Mater.* **9**, 2100137 (2021).

91. Wu, S. et al. Ratiometric mechanoluminescence in single Pr^{3+}-activated $LiGa_5O_8$. *Luminescence* **38**, 1465–1476 (2023).

92. Somakumar, A K. et al. High-pressure near-infrared luminescence studies of Fe^{3+}-activated $LiGaO_2$. *Inorg. Chem.* **62**, 12434–12444 (2023).

93. Xiao, Y. et al. Defect-management-induced multi-stimulus-responsive mechanoluminescence in Mn^{2+} doped gallate compound. *Nano Energy.* **120**, 109086 (2024).

94. Shao, P. et al. Near-infrared mechanoluminescence from Cr^{3+}-doped spinel nanoparticles for potential oral diseases detection. *Small.* **20**, 2402352 (2024).

95. Zhou, Z. et al. Multicolor mechanoluminescence from $Lu_3Al_2Ga_3O_{12}$:Tb, Eu for stress and temperature visual sensing. *Adv. Opt. Mater.* **13**, 2401993 (2025).

96. Zhang, J. C. et al. Discovering and dissecting mechanically excited luminescence of Mn^{2+} activators via matrix microstructure evolution. *Adv. Funct. Mater.* **31**, 2100221 (2021).

97. Wang, Z. et al. Stress-induced multi-stimulus-responsive mechanoluminescence in Mn^{2+} doped double perovskite compound. *Adv. Opt. Mater.* **12**, 2301796 (2024).

98. Wang, M. et al. Advanced luminescence anticounterfeiting based on dynamic photoluminescence and non-pre-irradiation mechanoluminescence. *Inorg. Chem.* **61**, 2911–2919 (2022).

99. Wu, S. et al. Regulating broadband near-infrared mechanoluminescence via energy-level engineering for potential biomechanical imaging. *Laser Photonics Rev.* **19**, 2401441 (2025).

100. Xiao, B. et al. Broadband near-infrared mechanoluminescence in Cr^{3+} doped $Mg_3Ga_2GeO_8$. *Chem. Eng. J.* **498**, 155040 (2024).

101. Luo, S. et al. High-stability near-infrared luminescent glass ceramic and its applications. *ACS Appl. Mater. Interfaces.* **16**, 45189–45196 (2024).

102. Zhang, Z. et al. Characterization and luminescence properties of $CaMgGe_2O_6$:Mn^{2+} NIR-I

mechanoluminescence phosphor. *J. Mater. Sci.:Mater. Electron.* **35**, 1–12 (2024).

103. Zhao, H., Wang, X., Li, J., Li, Y. & Yao, X. Strong mechanoluminescence of $Zn_2(Ge_{0.9}Si_{0.1})O_4$:Mn with weak persistent luminescence. *Appl. Phys. Express.* **9**, 012104 (2015).

104. Zheng, T. et al. Persistent photoluminescence and mechanoluminescence of a highly sensitive pressure and temperature gauge in combination with a 3D-printable optical coding platform. *Adv. Sci.* **11**, 2408686 (2024).

105. Luo, J. et al. Modulating smart mechanoluminescent phosphors for multistimuli responsive optical wood. *Adv. Sci.* **11**, 2305066 (2024).

106. Yan, Y. et al. Trap-regulated highly efficient mechanoluminescence and persistent mechanoluminescence of $Ca_2MgSi_2O_7:Eu^{2+}$. *J. Mater. Chem. C.* **11**, 11509–11517 (2023).

107. Tiwari, G. et al. Sahu IP. $Ca_2Al_2SiO_7:Ce^{3+}$ phosphors for mechanoluminescence dosimetry. *Luminescence.* **31**, 1479–1487 (2016).

108. Zhang, H., Terasaki, N., Yamada, H. & Xu, C. N. Mechanoluminescence of europium-doped $SrAMgSi_2O_7$ (A=Ca,Sr,Ba). *Jpn. J. Appl. Phys.* **48**, 04C109 (2009).

109. Zhang, L., Xu, C. N., Yamada, H. & Bu, N. Enhancement of mechanoluminescence in $CaAl_2Si_2O_8:Eu^{2+}$ by partial Sr^{2+} substitution for Ca^{2+}. *J. Electrochem. Soc.* **157**, J50 (2010).

110. Wang, Q. et al. Trap-controllable near-ultraviolet elastico-mechanoluminescence of Ce^{3+} doped phyllosilicate with melilite-type structure. *Opt. Express.* **32**, 22551–22562 (2024).

111. Huan, J. et al. Intense green mechanoluminescence from rare-earth doped gallium gehlenite for multimode anti-counterfeiting. *Mater. Res. Bull.* **174**, 112725 (2024).

112. Wu, S. et al. Multiple defect-induced high-resolution near-infrared mechanoluminescent materials for non-destructive detection of blood glucose and lipids. *Adv. Mater.* **36**, 2408508 (2024).

113. Zhang, J. C., Long, Y. Z., Yan, X., Wang, X. & Wang, F. Creating recoverable mechanoluminescence in piezoelectric calcium niobates through Pr^{3+} doping. *Chem. Mater.* **28**, 4052–4057 (2016).

114. Pan, C. et al. Trap-controlled mechanoluminescence in Pr^{3+}-activated $M_2Nb_2O_7$(M=Sr, Ca) isomorphic perovskites. *Opt. Mater. Express.* **8**, 1425–1434 (2018).

115. Zhang, J. C. et al. Achieving thermo-mechano-opto-responsive bitemporal colorful luminescence via multiplexing of dual lanthanides in piezoelectric particles and its multidimensional anticounterfeiting. *Adv. Mater.* **30**, 1804644 (2018).

116. Tu, D. et al. $LiNbO_3$: Pr^{3+} a multipiezo material with simultaneous piezoelectricity and sensitive piezoluminescence. *Adv. Mater.* **29**, 1606914 (2017).

117. Xiong, P. & Peng, M. Near infrared mechanoluminescence from the Nd^{3+} doped perovskite $LiNbO_3$:Nd^{3+} for stress sensors. *J. Mater. Chem. C.* **7**, 6301–6307 (2019).

118. Wang, C. et al. Interface-mediated mechanoluminescence enhancement from heterojunction phosphors: experiment and theory. *ACS Appl. Mater. Interfaces.* **15**, 30891–30901 (2023).

119. Yang, H. et al. Microstrain-stimulated elastico-mechanoluminescence with dual-mode stress sensing. *Adv. Mater.* **36**, 2401296 (2024).

120. Li, X., Hu, R., Wang, X., Li, Y. & Yao, X. Intense mechanoluminescence and photostimulated luminescence with less afterglow in Pr^{3+}/Gd^{3+} co-doped $LiTaO_3$ phosphors. *J. Lumin.* **238**, 118222 (2021).

121. Wang, X., Xu, C. N., Yamada, H., Nishikubo, K. & Zheng, X. G. Electro-mechano-optical conversions in Pr^{3+}-doped $BaTiO_3$-$CaTiO_3$ ceramics. *Adv. Mater.* **17**, 1254–1258 (2005).

122. Zhang, J. C., Wang, X., Yao, X., Xu, C. N. & Yamada, H. Strong elastico-mechanoluminescence in diphase (Ba, Ca)TiO_3: Pr^{3+} with self-assembled sandwich architectures. *J. Electrochem. Soc.* **157**, G269 (2010).

123. Zhang, J. C., Wang, X. & Yao, X. Enhancement of luminescence and afterglow in $CaTiO_3$:Pr^{3+} by Zr substitution for Ti. *J. Alloys Compd.* **498**, 152–156 (2010).

124. Kamimura, S., Yamada, H. & Xu, C. N. Strong reddish-orange light emission from stress-activated $Sr_{n+1}Sn_nO_{3n+1}$:Sm^{3+} (n= 1, 2, ∞) with perovskite-related structures. *Appl. Phys. Lett.* **101**, 9 (2012).

125. Lei, B., Man, S.Q., Liu, Y. & Yue, S. Luminescence properties of Sm^{3+}-doped $Sr_3Sn_2O_7$ phosphor. *Mater. Chem. Phys.* **124**, 912–915 (2010).

126. Bing, L., Song, Y., Yong, Z. & Ying, L. Luminescence properties of Sr_2SnO_4:Sm^{3+} afterglow phosphor. *Chin. Phys. Lett.* **27**, 037201 (2010).

127. Wang, Y., Huang, F. T., Luo, X., Gao, B. & Cheong, S. W. The first room-temperature ferroelectric sn insulator and its polarization switching kinetics. *Adv. Mater. (Deerfield Beach, Fla)* **29**, 2 (2016).

128. Xiong, P., Peng, M., Cao, J. & Li, X. Near infrared mechanoluminescence from $Sr_3Sn_2O_7:Nd^{3+}$ for in situ biomechanical sensor and dynamic pressure mapping. *J. Am. Ceram. Soc.* **102**, 5899–5909 (2019).

129. Tu, D., Hamabe, R. & Xu, C. N. Sustainable mechanoluminescence by designing a novel pinning trap in crystals. *The Journal of Physical Chemistry C.* **122**, 23307–23311 (2018).

130. Li, W. et al. Near-infrared dual-modal sensing of force and temperature in total knee replacement using mechanoluminescent phosphor of $Sr_3Sn_2O_7$:Nd, Yb. *Small.* **20**, 2310180 (2024).

131. Fang, H., Qiu, G., Wang, X., Li, Y. & Yao, X. Trap modification and mechanoluminescence improvement by Si substitution for Sn in $Sr_2SnO_4:Sm^{3+}$ ceramics. *J. Adv. Dielectr.* **8**, 1850016 (2018).

132. Zhao, T. et al. Rate-dependent mechanoluminescence in $SrZn_2S_2O:Mn^{2+}$ for time-characterized optoelectronic Devices. *The Journal of Physical Chemistry C*. **129**, 4715–4723 (2025).

133.Akiyama, M., Xu, C.N. & Nonaka, K. Intense visible light emission from stress-activated ZrO_2:Ti. *Appl. Phys. Lett.* **81**, 457–459 (2002).

134. Tong, J. et al. Significantly enhanced mechanoluminescence from Nb^{5+} co-doped $ZrO_2:Sm^{3+}$ via a high valence ion doping strategy. *J. Mater. Chem. C.* **11**, 11597–11605 (2023).

135. Suo, H. et al. A broadband near-infrared nanoemitter powered by mechanical action. *Matter.* **6**, 2935–2949 (2023).

136. Zhang, S. et al. Tunable full-color mechanoluminescence in rare earth-doped transparent amorphous glass. *Adv. Funct. Mater.* **34**, 2404439 (2024).

137. Li, X. et al. Irreversible $Ca_2B_2O_5$-based multicolor mechanoluminescence for security labels. *Adv. Mater. Technol.* **9**, 2301948 (2024).

138. Dou, C. et al. Self-recoverable and NIR-I to NIR-II tunable broadband mechanoluminescence of Cr^{3+}-doped antimonate double Perovskites. *Adv. Funct. Mater.*, 2419716 (2024).

139. Botterman, J., Van den Eeckhout, K., De Baere, I., Poelman, D. & Smet, P. F. Mechanoluminescence in $BaSi_2O_2N_2$:Eu. *Acta Mater.* **60**, 5494–5500 (2012).

140. Guo, X. et al. Trap-independent mechanoluminescence in $ZnB_2O_4:Mn^{2+}$/PDMS composite elastomer with self-recovery activity. *Chem. Phys. Lett.* **787**, 139235 (2022).

141. Ma, Z., Fang, S., Zhou, B., Yan, C. & Wang, Z. Trap-controlled, recoverable, and persistent mechanoluminescence for collision early-warning and mechanics displaying applications. *Adv. Mater. Technol.* **10**, 2401079 (2025).